Effect of target power density on the chemical composition, phase formation, and mechanical properties of MAX-phase Cr_2AlC coatings and prediction of mechanical properties of VAlN

Von der Fakultät für Georessourcen und Materialtechnik
der Rheinisch-Westfälischen Technischen Hochschule Aachen

zur Erlangung des akademischen Grades eines

Doktors der Ingenieurwissenschaften

genehmigte Dissertation

vorgelegt von **M.Sc. RWTH**

Holger Rueß

aus Esslingen am Neckar

Berichter: Univ.-Prof. Jochen M. Schneider, Ph.D.
Univ.-Prof. Dipl.-Ing. Dr. mont. Christian Mitterer

Tag der mündlichen Prüfung: 13. Dezember 2019

Materials Chemistry Dissertation

No.: 30 (2020)

Holger Rueß

Effect of target power density on the chemical composition, phase formation, and mechanical properties of MAX-phase Cr_2AlC coatings and prediction of mechanical properties of VAlN

Abstract

Huge progress has been made in the areas of material design and synthesis process development for protective coatings in the last decades. The common strategies for the industrial-scale deposition of multi-element containing coatings are based on reactive sputtering of elemental or multielement targets or based on non-reactive sputtering utilizing compound or composite targets. In both cases, it is desired to conserve either the elemental ratio of the target (reactive) or the whole target composition (non-reactive) in the coating. In case of non-reactive depositions, it is well-known, that the coating composition may drastically deviate from the target composition. To overcome this limitation, a methodology based on a combinatorial synthesis approach is derived within the first and second part of this thesis to enable the development of a processing parameter-dependent target composition, which furthermore allows to address application-related requirements (e.g. single-phase and dense coatings) for the synthesis of Cr_2AlC MAX-phase coatings by ion-assisted growth.

First, the effect of target power density, substrate bias potential and substrate temperature on the coating composition was studied. A Cr-Al-C composite target was sputtered utilizing direct current (DCMS: 2.3 W/cm^2) and high power pulsed magnetron sputtering (HPPMS: 373 W/cm^2) generators. At floating potential, all Cr-Al-C coatings showed similar compositions, independently of the applied target power density. However, as substrate bias potential was increased to -400 V, aluminum deficiencies by a factor of up to 1.6 for DCMS and 4.1 for HPPMS were obtained. Based on the measured ion currents at the substrate, preferential re-sputtering of Al is suggested to cause the dramatic Al depletion. As the substrate temperature was increased to

560 °C, the Al concentration was reduced by a factor of up to 1.9 compared to the room temperature deposition. This additional reduction may be rationalized by thermally induced desorption being active in addition to re-sputtering. Hence, it is evident that the composition of these films sputtered from the here employed composite target is strongly affected by the deposition conditions and that for a certain intended film composition - for example Cr_2AlC - a processing parameter specific composite target composition is required.

Secondly, to identify such a processing parameter specific composite target composition for the synthesis of the MAX-phase Cr_2AlC, which is indispensable for industrial application, a split $Cr_{0.46}$-$Al_{0.25}$-$C_{0.29}$ / $Cr_{0.15}$-$Al_{0.75}$-$C_{0.10}$ composite target was designed, which, due to the combinatorial approach, enables the compensation of the target power density and substrate bias potential induced Al-deficiencies. Furthermore, to utilize Cr_2AlC as protective coatings in nuclear, energy conversion or aerospace applications, several processing-related requirements need to be fulfilled. For example, the deposition process has to yield a dense and single-phase coating at substrate temperatures compatible with metallic substrates. Therefore, the effect of target power density and substrate bias potential on phase formation, microstructure evolution, and mechanical properties of sputtered Cr_2AlC coatings was studied. At a deposition temperature of 560 °C, DCMS and HPPMS were utilized. Generally, HPPMS resulted in coatings with superior density and hence larger elastic moduli compared to DCMS, indicating that ion bombardment by ionized film-forming species is beneficial. However, as the substrate bias potential was decreased to -200 V for DCMS and -100 V for HPPMS, the ion bombardment induced formation of the disordered $(Cr,Al)_2C_x$ solid solution was observed. It is evident that there is an optimum moderate ion energy for the formation of dense, single-phase Cr_2AlC MAX-phase coatings. Too small energy results in the formation of under-dense coatings. Too large energy results in the formation of the disordered $(Cr,Al)_2C_x$ solid solution in addition to the MAX-phase. Besides identifying an optimum processing window for the formation of Cr_2AlC coatings utilizing a split $Cr_{0.46}$-$Al_{0.25}$-$C_{0.29}$ / $Cr_{0.15}$-$Al_{0.75}$-$C_{0.10}$ composite target, the combinatorial synthesis approach furthermore enables the identification of the required processing parameter-dependent composite target composition for the deposition of stoichiometric Cr_2AlC coatings from a single-composition composite target.

In the third part of this thesis, the extensive and theoretically unexplained spread in experimentally obtained elastic moduli ranging from 254 to 599 GPa for $(V_{1-x}Al_x)_{1-y}N_y$, as reported in literature, was explored. To identify its origin, the effect of chemical composition ($0 \leq x \leq 0.75$), non-metal to metal ratio (N/M-ratio: $0.48 \leq y \leq 0.52$), and stress state ($-6 \leq \sigma \leq 2$ GPa) on the elastic modulus at room temperature was studied systematically by density functional theory employing the Debye-Grüneisen model. As the Al concentration is increased from $x = 0$ to $x = 0.75$, strong Al-N sp^3d^2 hybridization causes an increase in elastic modulus of 26 %. The effect of the N/M-ratio on the elastic properties is also Al content dependent. As y is increased from $y = 0.50$ to $y = 0.52$, decreasing bond distance upon vacancy formation causes an anomalous increase in the elastic modulus of 6 % for $V_{1-y}N_y$, while a decrease in elastic modulus of up to 5 % occurs for $(V_{1-x}Al_x)_{1-y}N_y$. A stress state variation from +2 to -6 GPa increases the elastic modulus e.g. for $(V_{0.5}Al_{0.5})_{0.5}N_{0.5}$ by 70 GPa and hence 13 % due to shifts in density of states towards lower energies implying bond strengthening. Thus, it is suggested that the extensive spread of 58 % in reported elastic moduli for

$(V_{1-x}Al_x)_{1-y}N_y$ can at least in part be rationalized based on variations in chemical composition, off-stoichiometry induced point defects, and stress state.

Zusammenfassung

In den letzten Jahrzehnten wurden enorme Fortschritte im Bereich des Materialdesigns und der Entwicklung von Syntheseverfahren für die Schutzschichtherstellung erzielt. Die gängige Strategie für die industrielle Abscheidung von Mehrelement-Schutzschichten basiert auf dem reaktiven Sputtern von Element- oder Multielementtargets oder auf dem nichtreaktiven Sputtern von Verbundtargets. In beiden Fällen ist es wünschenswert, entweder das vorliegende Elementverhältnis des Targets (reaktiv) oder die Gesamtzusammensetzung des Targets (nichtreaktiv) in den Schutzschichten beizubehalten. Allerdings ist es hinreichend bekannt, dass bei nicht-reaktiven Abscheidungen die Dünnschichtzusammensetzung drastisch von der Targetzusammensetzung abweichen kann. Um diese Einschränkung zu überwinden, wird im ersten und zweiten Teil dieser Arbeit eine Methodik abgeleitet, die auf einem kombinatorischen Syntheseansatz basiert und die Vorhersage einer prozessparameterabhängigen Targetzusammensetzung ermöglicht. Dadurch können anwendungsbezogene Anforderungen (z.B. einphasige und dichte Schutzschichten) für die Synthese von Cr_2AlC-MAX-Phasendünnschichten durch ionenunterstütztes Wachstum ermöglicht werden.

Als erstes wurde die Auswirkung der Targetleistungsdichte, des Substratbiaspotentials und der Substrattemperatur auf die chemische Zusammensetzung der Dünnschichten untersucht. Ein Cr-Al-C-Verbundtarget wurde unter Verwendung von Gleichstrom- (DCMS: 2,3 W/cm²) sowie gepulsten Hochleistungs-Magnetron-Sputter-Generatoren (HPPMS: 373 W/cm²) gesputtert. Bei Floating-Potential zeigen alle Cr-Al-C-Dünnschichten ähnliche Zusammensetzungen, unabhängig von der verwendeten

Targetleistungsdichte. Bei einer Erhöhung des Substratbiaspotentials auf bis zu -400 V wurden Aluminiumdefizite bis zu einem Faktor von 1,6 für DCMS und 4,1 für HPPMS beobachtet. Gemessene Ionenströme am Substrat lassen auf ein bevorzugtes Rücksputtern von Al, welches den drastischen Al-Verlust verursachen könnte, schließen. Bei einer Erhöhung der Substrattemperatur auf 560ºC verringert sich die Al-Konzentration im Vergleich zur Raumtemperaturbeschichtung um einen Faktor von bis zu 1,9. Dieser zusätzliche Al-Verlust kann dadurch erklärt werden, dass neben Rücksputtereffekten eine thermisch induzierte Desorption on Al auftritt. Diese Ergebnisse verdeutlichen, dass die Zusammensetzung der Dünnschichten, welche von dem hier verwendeten Verbundtarget gesputtert wurden, stark von den Abscheidungsbedingungen beeinflusst wird und dass für eine bestimmte beabsichtigte Dünnschichtzusammensetzung - beispielsweise Cr_2AlC - eine prozessparameter-spezifische Verbundtarget-Zusammensetzung erforderlich ist.

Da eine prozessparameterspezifische Targetzusammensetzung für eine industrielle Anwendbarkeit von Cr_2AlC-MAX-Phasendünnschichten unerlässlich ist, wurde in einem zweiten Schritt ein geteiltes $Cr_{0,46}$-$Al_{0,25}$-$C_{0,29}$ / $Cr_{0,15}$-$Al_{0,75}$-$C_{0,10}$-Verbundtarget entworfen, das aufgrund des kombinatorischen Ansatzes die Kompensation des targetleistungsdichte- und substratbiaspotentialinduzierten Al-Defizits ermöglicht. Um Cr_2AlC als Schutzschicht in Nuklear-, Energieumwandlungs- oder Luft- und Raumfahrtanwendungen einsetzen zu können, müssen mehrere verfahrenstechnische Anforderungen erfüllt sein. Beispielsweise muss der Beschichtungsprozess die Synthese einphasiger und dichter Schutzschichten bei Substrattemperaturen, die mit metallischen Substraten kompatibel sind, ermöglichen. Daher wurde der Einfluss der Targetleistungsdichte und des Substratbiaspotentials auf die Phasenbildung, die Mikrostrukturentwicklung und die mechanischen Eigenschaften gesputterter Cr_2AlC-Dünnschichten untersucht. Bei einer Beschichtungstemperatur von 560°C wurden DCMS und HPPMS verwendet. Im Allgemeinen weisen HPPMS-Beschichtungen eine höhere Dichte und damit einen größeren Elastizitätsmodul verglichen mit DCMS auf, was darauf hindeutet, dass ein Ionenbeschuss durch ionisierte filmbildende Spezies vorteilhaft ist. Wenn das Substratbiaspotential für DCMS auf -200 V und für HPPMS auf -100 V erhöht wird, kann die durch Ionenbeschuss induzierte Bildung des ungeordneten $(Cr,Al)_2C_x$-Mischkristalls beobachtet werden. Daraus wird ersichtlich, dass es eine optimale moderate Ionenenergie für die Bildung dichter einphasiger Cr_2AlC-MAX-Phasendünnschichten gibt. Eine zu geringe Energie führt zur Bildung von unterdichten Dünnschichten. Eine zu große Energie führt zur Bildung des ungeordneten $(Cr,Al)_2C_x$-Mischkristalls zusätzlich zur MAX-Phase Cr_2AlC. Neben der Identifizierung eines optimalen Prozessfensters für die Bildung von Cr_2AlC-Dünnschichten unter Verwendung eines geteilten $Cr_{0,46}$-$Al_{0,25}$-$C_{0,29}$ / $Cr_{0,15}$-$Al_{0,75}$-$C_{0,10}$-Verbundtargets ermöglicht der kombinatorische Syntheseansatz außerdem die Identifizierung der für die Abscheidung von stöchiometrischen Cr_2AlC-Dünnschichten notwendigen prozessparameterabhängige Verbundtargetzusammensetzung.

Im dritten Teil dieser Arbeit wird die beträchtliche und theoretisch ungeklärte Streuung der in der Literatur berichteten, experimentell gemessenen Elastizitätsmoduln von 254 bis 599 GPa für $(V_{1-x}Al_x)_{1-y}N_y$ untersucht. Um deren Ursprung zu identifizieren, wird der Einfluss der chemischen Zusammensetzung ($0 \leq x \leq 0{,}75$), des Nichtmetall-Metall-Verhältnisses (N/M-Verhältnis: $0{,}48 \leq y \leq 0{,}52$) und des Spannungszustands ($-6 \leq \sigma \leq 2$ GPa) auf den Elastizitätsmodul bei Raumtemperatur systematisch mittels

Dichtefunktionaltheorieberechnungen unter Verwendung des Debye-Grüneisen-Modells untersucht. Bei einer Erhöhung der Al-Konzentration von x = 0 auf x = 0,75 bewirkt eine starke Al-N (sp^3d^2)-Hybridisierung eine Zunahme des Elastizitätsmoduls um 26 %. Der Einfluss des N/M-Verhältnisses auf die elastischen Eigenschaften ist auch vom Al-Gehalt abhängig. Wenn y von y = 0,50 auf y = 0,52 erhöht wird, bewirkt die Bildung von Leerstellen eine Verringerung des Bindungsabstands und somit eine anomale Zunahme des Elastizitätsmoduls von 6 % für $V_{1-y}N_y$, während eine Abnahme des Elastizitätsmoduls von bis zu 5 % für $(V_{1-x}Al_x)_{1-y}N_y$ auftritt. Eine Spannungszustandsänderung von +2 auf -6 GPa erhöht den Elastizitätsmodul, z.B. für $(V_{0.5}Al_{0.5})_{0.5}N_{0.5}$ um 70 GPa und somit um 13 %. Dies lässt sich aufgrund von Verschiebungen in der Zustandsdichte in Richtung niedrigerer Energien erklären, was auf eine Zunahme der Bindungsstärke hindeutet. Diese Ergebnisse zeigen, dass die beträchtliche Streuung von 58 % der in der Literatur berichteten Elastizitätsmoduln für $(V_{1-x}Al_x)_{1-y}N_y$ zumindest teilweise durch Variationen in der chemischen Zusammensetzung, durch Punktdefekte verursachten Nichtstöchiometrie und des Spannungszustands erklärt werden können.

Preface

This work was supported by the German Research Foundation in the frameworks of the collaborative research center SFB-TR87 and SPP 1568 SCHN 735/19-2 as well as by Plansee Composite Materials GmbH, which are gratefully acknowledged. Density functional theory calculations were performed with computing resources granted by JARA-HPC from RWTH Aachen University under project JARA0131 and JARA0151.

The following papers contributed to this thesis:

Paper I

HPPMS deposition from composite targets: Effect of two orders of magnitude target power density changes on the composition of sputtered Cr-Al-C thin films

H. Rueß, M. to Baben, S. Mráz, L. Shang, P. Polcik, S. Kolozsvári, M. Hans, D. Primetzhofer, and J.M. Schneider

Vacuum 145 (2017) 285

Paper II

Effect of chemical composition, defect structure, and stress state on the elastic properties of $(V_{1-x}Al_x)_{1-y}N_y$

H. Rueß, D. Music, A. Bahr, J.M. Schneider

Journal of Physics: Condensed Matter 32 (2020) 025901

Paper III

Effect of target peak power density on the phase formation, microstructure evolution and mechanical properties of Cr_2AlC MAX-phase coatings

H. Rueß, J. Werner, Y. Unutulmazsoy, J.W. Gerlach, X. Chen, B. Stelzer, D. Music, S. Koloszvári, P. Polcik, T.E. Weirich, J.M. Schneider

In manuscript

Contributions to the papers

Thin film depositions for paper I were done by HR with the help of MtB and LS and for paper III by HR. Chemical composition analysis for paper I was carried out by DP, MH, and HR and for paper III by HR. Mass spectroscopy measurements for paper I were performed by HR with the help of SM. X-ray diffraction for paper III was performed by YU, JWG, and HR and TEM measurements were carried out and interpreted by JW, TEW, and XC. Nanoindentation in paper III was done by BS and HR. *Ab initio* calculations in paper II were performed by AB, DM, and HR and in paper III by DM and HR. For all papers, goals were defined and strategies were developed with JMS. All co-authors took part in the discussion of the results and writing the manuscripts.

Publications related to the topic of this thesis:

Paper IV

Nonmetal sublattice population induced defect structure in transition metal aluminum oxynitrides

K.P. Shaha, H. Rueß, S.J. Rotert, M. to Baben, D. Music, and J.M. Schneider

Applied Physics Letters 103 (2013) 221905

Paper V

Unprecedented thermal stability of inherently metastable titanium aluminum nitride by point defect engineering

M. to Baben, M. Hans, D. Primetzhofer, S. Evertz, H. Rueß, and J.M. Schneider

Materials Research Letters 5 (2017) 158

Paper VI

Correlative plasma-surface model for metastable Cr-Al-N: Frenkel pair formation and influence of the stress state on the elastic properties

D. Music, L. Banko, H. Rueß, M. Engels, A. Hecimovic, D. Grochla, D. Rogalla, T. Brögelmann, A. Ludwig, A. von Keudell, K. Bobzin, and J.M. Schneider

Journal of Applied Physics 121 (2017) 215108

Paper VII

Analysis of the inhibition of thermal degradation of molten polycarbonate at tool steel interfaces by thin TiAlN coatings

M. Wiesing, T. los Arcos, M. to Baben, H. Rueß, J.M. Schneider, and G. Grundmeier

Polymer Degradation and Stability 143 (2017) 196

Paper VIII

Extended metastable Al solubility in cubic VAlN by metal-ion bombardment during pulsed magnetron sputtering: Film stress vs subplantation

G. Greczynski, S. Mráz, H. Rueß, M. Hans, J. Lu, L. Hultman, and J.M. Schneider

Journal of Applied Physics 122 (2017) 025304

Paper IX

From quantum to continuum mechanics: Studying the fracture toughness of transition metal nitrides and oxynitrides

J. Gibson, S. Rezaei, H. Rueß, M. Hans, D. Music, S. Wulfinghoff, J.M. Schneider, S. Reese, and S. Korte-Kerzel

Materials Research Letters 6 (2018) 142

Paper X

Synthesis, crystal structure, microstructure and mechanical properties of $(Ti_{1-x}Zr_x)_3SiC_2$ MAX phase solid solutions

L. Qu, G. Bei, B. Stelzer, H. Rueß, J.M. Schneider, D. Cao, S. van der Zwaag, and W.G. Sloof

Ceramics International 45 (2019) 1400

Paper XI

Spinodal decomposition of reactively sputtered $(V_{0.64}Al_{0.36})_{0.49}N_{0.51}$ VAlN thin films

M. Hans, H. Rueß, Z. Czigány, J. Krause, P. Ondračka, D. Music, S. Evertz, D.M. Holzapfel, D. Primetzhofer, and J.M. Schneider

Surface and Coating Technology 389 (2020) 125641

Paper XII

How tensile tests allow a screening of the fracture toughness of hard coatings

B. Völker, C. Du, H. Fager, H. Rueß, R. Soler, C. Kirchlechner, G. Dehm, and J.M. Schneider

Surface and Coating Technology 390 (2020) 125645

Paper XIII

Quantum-mechanical study of interaction between polycarbonate and $M_{0.5}Al_{0.5}N(001)$ surfaces (M = Ti, V, Cr)

D. Music, H. Rueß, and J.M. Schneider

Applied Surface Science 520 (2020) 146306

Other publications:

Paper XIV

Stiffness and toughness prediction of Co–Fe–Ta–B metallic glasses, alloyed with Y, Zr, Nb, Mo, Hf, W, C, N and O by ab initio molecular dynamics

V. Schnabel, S. Evertz, H. Rueß, D. Music, and J.M. Schneider

Journal of Physics Condensed Matter 27 (2015) 105502

Paper XV

Chemical composition and stress dependence of the elastic properties of κ-$(Fe,Mn)_3AlC$ thin films

F. Herrig, D. Music, H. Rueß, A.L. Ravensburg, P.J. Pöllmann, and J.M. Schneider

Scripta Materialia 153 (2018) 49

Paper XVI

Transition Metal-Carbon Bond Enthalpies as Descriptor for the Electrochemical Stability of Transition Metal Carbides in Electrocatalytic Applications

D. Göhl, H. Rueß, M. Pander, A.R. Zeradjanin, K.J.J. Mayrhofer, J.M. Schneider, A. Erbe, and M. Ledendecker

Journal of The Electrochemical Society 167 (2020) 021501

Paper XVII

Stable and Active Oxygen Reduction Catalysts with Reduced Noble Metal Loadings through Potential Triggered Support Passivation

D. Göhl, H. Rueß, S. Schlicht, A. Vogel, M. Rohwerder, K.J.J. Mayrhofer, J. Bachmann, Y. Román-Leshkov, J.M. Schneider, and M. Ledendecker

ChemElectroChem 7 (2020) 2404

Acknowledgments

An erster Stelle möchte ich mich bei meinem Betreuer Prof. Jochen Schneider bedanken. Vielen Dank für deine hervorragende Betreuung, die vielen konstruktiven Diskussionen, dein Vertrauen und die vielen Freiheiten, die du mir während meiner Promotion gegeben hast.

An zweiter Stelle möchte ich mich bei Prof. Christian Mitterer für die vielen hilfreichen Diskussionen und Ratschläge während der großartigen Doktorrandenseminare in Leoben, Kitzeck und Aachen bedanken.

Besonderer Dank gilt euch, Denis und Stano. Ihr standet mir während meiner gesamten siebeneinhalb Jahre am MCh immer hilfsbereit zur Seite, habt mich an die Quantenmechanik und das Magnetronsputtern herangeführt und mir mit eurer positiven Herangehensweise immer einen Weg durch jede noch so komplexe wissenschaftliche Fragestellung gezeigt.

Des Weiteren möchte ich mich bei all meinen Kollegen und Studenten für die großartige Zeit am MCh bedanken. Vielen Dank für eure Unterstützung und die ständige Bereitschaft zu helfen. Die offene und familiäre Atmosphäre als auch die vielen gemeinsamen Diskussionen haben meine Zeit am MCh bereichert.

Außerdem bedanke ich mich bei allen Projektpartnern für die vielen interessanten Diskussionen und Einblicke in andere Themenbereiche sowie in die industrielle Anwendung.

Abschließend gilt mein Dank meiner Familie, meiner Freundin und Freunden für den uneingeschränkten Rückhalt und die Unterstützung während meiner Promotion.

Table of content

1. Introduction

Thin films and coatings are ubiquitous in our everyday life, be it in electronic, medical, or optical devices, in the transportation and energy generation sector, or in industrial fabrication processes. They modify the surface properties of a material, e.g. increase the hardness and stiffness, lower the friction coefficient, increase corrosion and oxidation resistance, and/ or lower adhesion or sticking ability in contact with other materials. This enables them to be utilized as wear protective coatings for tools or other heavily loaded components. Owing to their broad utilization and, hence, to the requirement to possess tailored properties for this wide range of applications, a variety of different material systems have been designed and engineered over the last decades. Magnetron sputtering, among various other physical vapor deposition techniques, is widely used to synthesize this variety of different multi-element containing compound coatings.

The industrial-scale deposition of multi-element containing coatings can, in principle, be achieved by co-sputtering from several elemental targets or by sputtering from a compound or composite target. The utilization of compound or composite targets is attractive from an industrial application point of view due to process simplicity, improved repeatability [1] and a more homogeneous coating composition [2]. The desired coating composition usually corresponds to the target composition. However, coatings deposited from multi-element targets often exhibit a considerable compositional deviation to the desired target composition. These compositional deviations stem from differences in emission angles and energy distributions [3-5], gas phase scattering behavior [6-8], sticking probabilities [5, 9-13], preferential re-sputtering [5, 9-13] and selective evaporation behavior [1, 14-16] of the individual target constituents. In particular, targets containing constituents with significant mass differences, such as TiB [3, 7], TiW [5, 9-13], WB [17], SiC [18], MoSi [19, 20], VC [21], NbC [22], V-Al-C [23], Cr-Al-C [4, 24], Ti_2AlC [14, 25], Ti_3SiC_2 [8, 15, 26], Mo-Al-Ti [27], and Mo-B-C [28], are prone to drastic deviations between the target and film composition (Figure 1), which e.g. may prevent the desired phase formation, as observed for the MAX-phases Ti_3SiC_2 [15, 26] and Cr_2AlC [24].

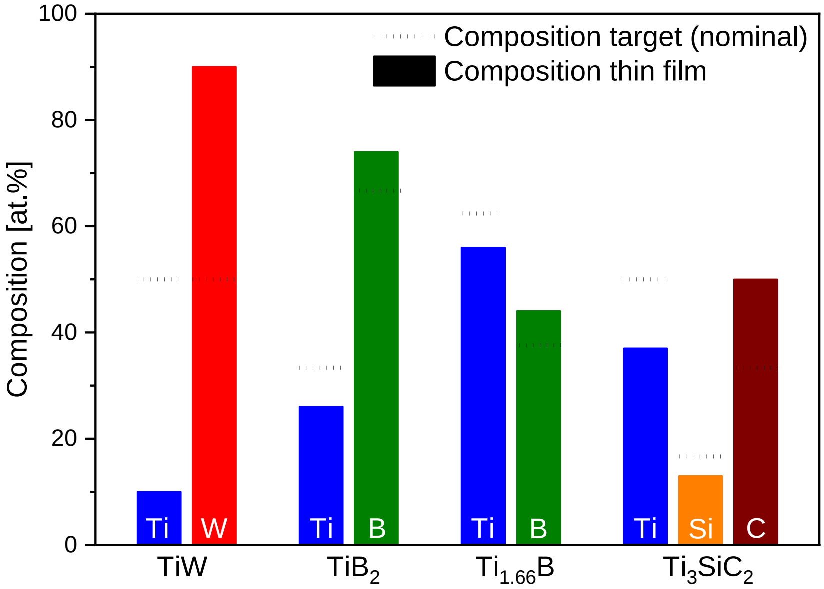

Figure 1: Compositional deviations between target (dotted line) and coatings (bars) for TiW [13], TiB_2 [7], $Ti_{1.66}B$ [3], and Ti_3SiC_2 [15].

MAX-phases (space group $P6_3/mmc$) are hexagonal nanolayered ternary metal carbides or nitrides with the general formula $M_{n+1}AX_n$, where n is 1-3, M is an early transition metal, A is an A-group element, and X is either C or N [1, 29]. These nanolaminates exhibit alternating metallic-like layers (between M and A) and ceramic-like layers (between M and X) resulting in a unique set of metallic and ceramic properties such as high stiffness [30, 31] and damage tolerance [32], good machinability [33], high thermal shock [34] and corrosion resistance [35], electrical conductivity [31], and even show potential as self-healing materials [36-38]. These unique properties make MAX-phases potential candidates for industrial applications in the fields of protective coatings (nuclear or aerospace applications [38-40]) and high temperature electrical contacts [29]. Several challenges for the applicability of Cr_2AlC MAX-phase coatings for industrial applications using direct current magnetron sputtering (DCMS) have been addressed in the past: The deposition of single-phase coatings, the homogeneous deposition over large areas utilizing compound targets, and the deposition at low substrate temperatures [2]. Another critical challenge, controlling the coating´s microstructure by ion assisted growth has only been recently addressed by either utilizing high energetic deposition such as high power pulsed magnetron sputtering (HPPMS) using co-sputtering from three elemental targets [41], which is not feasible for industrial applications or by applying a substrate bias while sputtering a Cr_2AlC compound target using DCMS [24], which resulted in the formation of impurity phases possibly due to pronounced compositional deviations between target and coating.

It was shown for DCMS, that the magnitude of compositional deviation between target and coating depends on the pressure-to-distance product [3, 4, 8], the substrate bias potential [3, 5, 12, 13] and the deposition temperature [1, 14-16]. Additionally to these parameters, the effect of HPPMS, a technique employing target peak power densities on the order of kW/cm^2 [42], thus, leading to a significantly higher fraction of ionized sputtered material [43] compared to DCMS, on compositional deviations between compound or composite targets and deposited coatings has yet not been systematically studied. However, synthesis reports of Ti_3SiC_2 [26] and V_2AlC [23] from compound/ composite targets by HPPMS suggest compositional deviations with respect to the target composition.

Beside causing compositional deviation between composite or compound targets and coatings, the pressure-to-distance product, the substrate bias potential, the substrate temperature, and the target power density define the energetic conditions during growth and thus affect the formation of defects, intrinsic stresses, compositional phase formation range, grain size, or preferred orientation, which, additionally to the chemical composition, define the coating properties. Owing to this complexity and the extremely challenging experimental approach to identify the magnitude of those individual contributions on coating properties (e.g. elastic properties), *ab initio* calculations can be employed to gain an insight and a fundamental understanding of the dominant physical mechanisms. This has been demonstrated for example for TiAlN [44] and CrAlN [45], which belong to the group of metastable NaCl-structured transition metal aluminum nitrides (space group $Fm\bar{3}m$). These hard coatings have widely been applied in industry over the last 30 years [46] for cutting and forming applications due to their excellent property combinations, such as high hardness and stiffness [47, 48], low wear [49], and good oxidation and corrosion resistance [49, 50]. $V_{1-x}Al_xN$, a less explored isostructural system, crystalizes up to a critical Al solubility limit x in a single phase and metastable NaCl structure. Above this critical solubility limit, the precipitation of thermodynamically stable and softer wurtzite (w) AlN occurs. Thermodynamically stable binary counterparts cubic VN and w-AlN are insoluble under thermodynamic equilibrium conditions so that no ternary phase diagram exists and explorations are only feasible employing non-equilibrium synthesis techniques. VAlN has recently gained attention as wear-resistant coating for deep drawing of high strength steels due to the combination of high hardness and low friction coefficient [51, 52], its unprecedented high Al solubility of x = 0.75 [53], and its predicted high bulk (B = 279 – 285 GPa [54-56] for x = 0.5) and elastic (Young´s) modulus (E = 482 – 492 GPa [55, 56] for x = 0.5), which are larger compared to those of $Ti_{0.5}Al_{0.5}N$ (E = 463 – 472 GPa [32, 55]) and $Cr_{0.5}Al_{0.5}N$ (E = 375 GPa [47]). However, for $(V_{1-x}Al_x)_{1-y}N_y$ an extensive and theoretically unexplained spread in experimentally obtained elastic moduli ranging from 254 to 599 GPa is reported in literature [55-59].

The above-mentioned challenges in the field of industrial-scale synthesis and synthesis-property relationships of multi-element containing protective coatings are addressed in chapters 3, 4, and 5 and can be summarized as follows:

I) Understanding the effect of target power density, substrate bias potential, and substrate temperature on the composition of industrial-scale sputtered Cr-Al-C multi-element containing coatings from a $Cr_{0.50}$-$Al_{0.27}$-$C_{0.23}$ composite target.

II) Understanding the influence of target power density and substrate bias potential on the phase formation, microstructure evolution, and mechanical properties of industrial-scale sputtered Cr_2AlC MAX-phase.

III) Deriving a methodology to identify the required processing parameter-dependent composite target composition for the deposition of stoichiometric Cr_2AlC coatings.

IV) Understanding the origin of the extensive and theoretically unexplained spread in experimentally obtained elastic moduli for $(V_{1-x}Al_x)_{1-y}N_y$.

2. Methods

This chapter comprises a short introduction into thin film deposition and characterization techniques as well as into the utilized theoretical methods, which were used within this thesis.

2.1. Thin film deposition

2.1.1 Magnetron sputtering

Magnetron sputtering belongs to physical vapor deposition (PVD) methods, which are used to synthesize thin films by condensation of vaporized target material onto various substrates. Magnetron sputtering can be differentiated from other PVD techniques, such as evaporation, cathodic arc evaporation, or pulsed laser deposition (PLD) via the ionization degree of the ejected target material. The ionization degree of film-forming species ranges from a few percent for DCMS [60] to 70 - 90 % for HPPMS [43, 61]. Cathodic arc evaporation [62] and PLD [63] are characterized by an ionization degree of film-forming species of up to 100 %.

The thin film growth process utilizing magnetron sputtering consists of three stages: Ejection of the target material by high energetic particle bombardment (sputtering), transport of the sputter species from the target through the gas phase, and finally the condensation onto various substrates. The target is negatively biased, consequently positively charged ions from the plasma are accelerated towards the target due to the potential difference between plasma and target. These ions impinge onto the target surface, induce a collision cascade by which target atoms and secondary electrons are emitted. The (secondary) electrons are trapped in the vicinity of the target by the magnetic field, ionize the gas and/or sputtered target atoms and, hence, enable sustaining the plasma. The sputtered target atoms and part of the generated target ions leave the vicinity of the target, are transported through the plasma and, eventually, condense with a material dependent probability (sticking coefficient) on a substrate and, thereby, form a film. The condensation of the film-forming species decisively determines the properties of the growing thin films such as the crystallinity, texture, morphology, residual stress state, etc. and is mainly governed by the energetic conditions at the substrate. Thus, a precise control of energetic conditions at the substrate is essential, which can be accomplished by heating the substrate, which transfers energy to the film-forming species (adatoms) and, hence, enables surface or bulk diffusion. Another source of energy are the impinging plasma particles (inert gas atoms and ions as well as film-forming atoms and ions) onto the substrate. While the energy of film-bombarding atoms is inherently determined by the sputter process and transport, the energy of ions can be manipulated by an electrical field caused by an applied substrate bias potential. Two scenarios can be distinguished based on the ion-to-neutral ratio of the film-forming species flux. In case of a low ion-to-neutral ratio flux (DCMS), the main energy input into the growing thin film stems from inert gas ion bombardment, which is defined by the energy transfer from inert gas ions to the adatoms and can be calculated by the energy transfer function [64]

(1) $$\frac{E_a}{E_i} = \frac{4M_aM_i}{(M_i+M_a)^2}cos^2\theta,$$

where θ is the angle of incidence, E_i and E_a are the energies of the incident particles and adatoms, respectively, and M_i and M_a are the masses of the incident particles and adatoms, respectively. Due to mass differences between the inert gas ions and adatoms, the energy transfer is not ideal. For a high ion-to-neutral ratio flux (HPPMS), where the main energy input stems from film-forming ions, the energy transfer from impinging film-forming species to adatoms is ideal and furthermore not necessarily required, as impinging film-forming species may become highly mobile adatoms directly. Thus, the energy input from film-forming species is more effective compared to inert gas ion bombardment.

DCMS:

In DC magnetron sputtering, the cathode (target) is connected to a direct current (DC) power supply and a constant negative direct current is applied. DCMS is characterized by a relatively low plasma density and, hence, by a low ion-to-neutral ratio of the sputtered particle flux due to the limited power densities of several tens W/cm^2, which can be applied to the target. The limit originates from the maximum thermal load, which a target can endure before it overheats and/or, eventually, melts.

HPPMS:

High power pulsed magnetron sputtering, a technique employing peak target power densities on the order of kW/cm^2 has first been introduced by Kouznetsov *et al.* in 1999 [43]. To differentiate HPPMS from DCMS and pulsed DCMS, the target peak power density typically exceeds the time-averaged power density by two orders of magnitude [65].

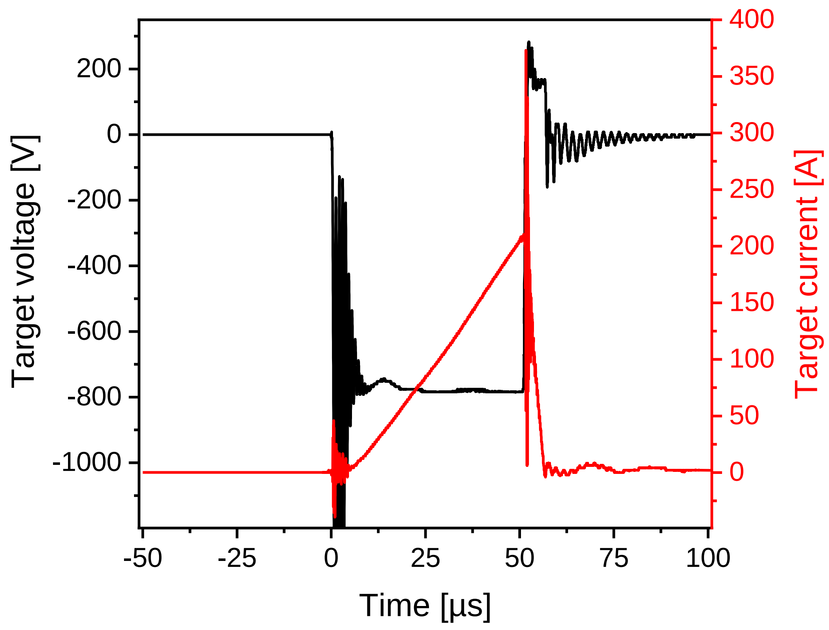

Figure 2: Temporal evolution of target voltage and current during a 50 µs long HPPMS pulse with a duty-cycle of 1.25 % recorded for a Cr_2AlC depositions.

It is characterized by high plasma densities and hence ion-to-neutral ratios, which is achieved by the utilization of high target peak power densities. To avoid target damage by overheating, the power is usually applied in 5 − 200 µs long pulses with frequencies of tens of Hz to kHz, so that the time-averaged power densities are in the range of those used for DCMS. Figure 2 shows a characteristic HPPMS pulse with a duration of 50 µs and a duty-cycle of 1.25 % from a Cr_2AlC deposition and is characterized by a constant pulse voltage of -800 V and a linearly increasing current with time reaching 200 A at the end of the pulse.

2.1.2 Multi-component thin films

To synthesize multi-component thin films, such as MAX-phases (e.g. Cr_2AlC), TMAl(O)N (transition metal, TM = Ti, V, Cr) or high entropy alloys (e.g. TiZrHfVNbTaCrMoW) by magnetron sputtering, the required elements need to be supplied. Some elements can be provided by reactive gases, e.g. nitrogen (N_2), oxygen

(O_2), or carbon (CH_4), while many elements need to be provided by the sputtering target(s). Elemental or multi-element containing targets (powder metallurgical composite or compound targets) can be utilized. From an industrial point of view, utilization of elemental targets is not desirable, as co-sputtering from several targets would be required for the synthesis of multi-elemental thin films, hence, limiting the choice to multi-element containing targets. However, the chemical composition of thin films deposited from multi-element containing targets may deviate from the target composition, such as for TiB [3, 7], TiW [5, 9-13], WB [17], SiC [18], MoSi [19, 20], VC [21], NbC [22], V-Al-C [23], Cr-Al-C [4], Ti_2AlC [14, 25], Ti_3SiC_2 [8, 15, 26], Mo-Al-Ti [27], Mo-Al-C [28], YBaCuO [66], and CuZnSnSe [67]. The underlying origin can be found within the three stages of deposition process:

(1) Sputtering: Different angular and energy distributions of individual target species in the sputtered flux [3, 4, 19, 20, 28, 68]; Non-steady state of the target composition [66].

(2) Transport: Element-specific transport through the gas phase due to mass-dependent differences in gas phase scattering behavior of individual target species associated with the mean free path, the energy transfer coefficient, the collision cross-sections, and the scattering angle [3-7, 68].

(3) Condensation: Different sticking coefficients of film-forming species [9]; Preferential re-sputtering of the film constituents [5, 9-13]; Evaporation of selected film constituents [14].

2.1.3 Plasma analysis

Thin film growth and, hence, the film properties are highly dependent on the plasma chemistry and energetics, as discussed in section 2.1.1. Thus, knowing the type, flux, and energy of the plasma species is essential. This information can be obtained for example by mass spectrometry.

Mass spectrometry

The operation principle of an energy-resolved mass spectrometer is based on the separation of ions according to their mass-to-charge ratio. It consists of an extraction orifice (limiting the amount of plasma species entering the mass spectrometer), sometimes an ion source (enables the measurement of plasma neutrals by ionizing them), an energy filter (separates ions according to their energy-to-charge ratio), a mass filter (separates ions according to their mass-to-charge ratio), and an ion detector (ion counter). The obtained results are either a mass spectrum, a plot of intensity vs. mass-to-charge ratio, or an ion energy distribution function (IEDF), as shown in Figure 3.

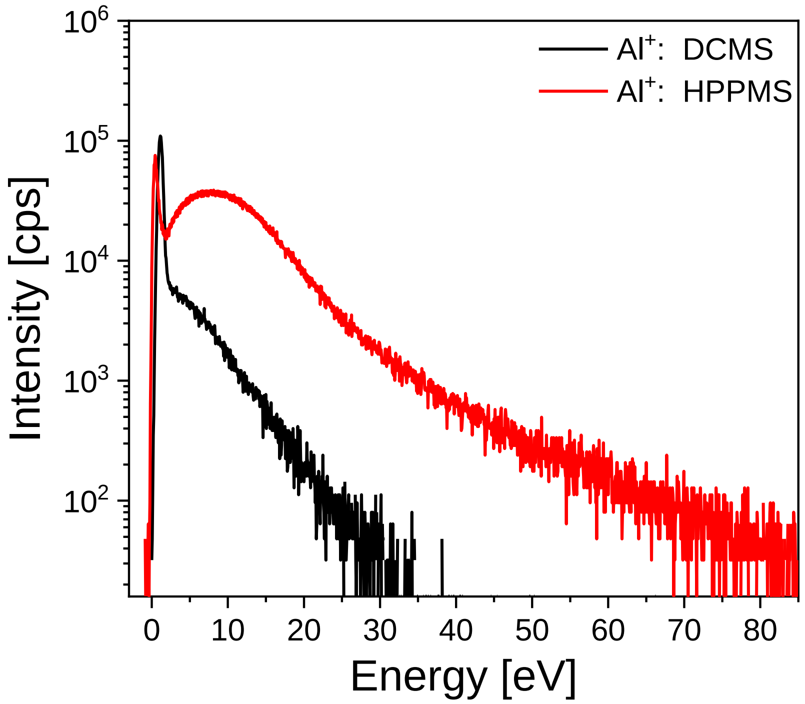

Figure 3: Ion energy distribution function (IEDF) of Al^+ ions measured during a Cr_2AlC deposition utilizing DCMS (black) and HPPMS (red).

Based on IEDFs, the energy fluxes of ions present in the plasma can be calculated based on

(2) $$\text{Energy flux} = \int \left(\text{E x IEDF(E)}\right) \text{dE},$$

where *E* is the ion energy and the IEDF is the ion energy distribution function. More information can be found in [69].

2.2. Thin film characterization

2.2.1 Chemical compositional analysis

<u>Energy dispersive X-ray spectroscopy</u>

Energy dispersive X-ray spectroscopy (EDS or EDX) is the most common technique to analyze the chemical composition of thin films. Its principle is based on the detection of characteristic X-rays from the specimen elements, which are generated by focusing an electron beam onto the sample. These primary electrons may eject an inner shell electron of a specimen atom, which is subsequently filled by an outer shell electron. The corresponding energy difference between these electron shells is emitted as a characteristic X-ray quant and is detected by the EDX detector. By separating the energies and counting the amount of detected characteristic X-ray quants, a spectrum is obtained revealing the composition of the specimen. Further details can be found in [70].

Elastic recoil detection analysis:

Time-of-flight elastic recoil detection analysis (ToF-ERDA) belongs to the ion beam-based characterization techniques for compositional analysis and is mostly used for the quantification of samples containing light elements, such as boron, carbon, nitrogen, or oxygen. Its principle is based on the detection of recoils from a sample, which are generated by irradiating the specimen with highly ionized isotopes (e.g. iodine) with energies in the MeV range. A mass-dependent depth profile is obtained by measuring the flight-time of the recoils and the number of detected recoils is proportional to their concentration in the specimen. Further information can be found in [71].

2.2.2 Structural analysis

X-ray diffraction:

X-ray diffraction (XRD) can be used to examine the crystal structure and to determine the lattice parameters, the residual stress state, texture, or grain size of a material. Its principle is based on the detection of diffracted X-rays on crystal planes. For polycrystalline materials, a monochromatized X-ray beam is radiated onto a sample and is subsequently scattered there. Constructive interference is obtained when Bragg´s law

(3) $$2d sin\theta = n\lambda$$

is fulfilled, where *d* is the lattice spacing, θ is the scattering angle, *n* is an integer number and λ is the X-ray wavelength. In case of constructive interference, intensity peaks are obtained, which can be displayed in a diffractogram (intensity vs. 2θ). More details can be found in [72].

Transmission electron microscopy

Transmission electron microscopy (TEM) is used to study the microstructure as well as spatially-resolved crystal structure on a nanometer-scale in a transmission geometry. Electrons are accelerated to energies of several 100 keV and are transmitted through a very thin lamella (typically < 50 nm), which can be prepared using focused ion beam (FIB) techniques. The electron beam is scattered and/or diffracted within the lamella. For microstructural imaging, the scattered electrons are considered and depending on the selected operation mode, either the scattered electrons are used for imaging (dark-field mode) while the unscattered (transmitted) electrons are blocked or *vice versa* (bright-field mode). In order to determine the spatially-resolved crystal structure, the diffracted electrons are considered, which is called selected area electron diffraction (SAED).

2.2.3 Mechanical properties

Local mechanical properties of thin films such as elastic (Young´s) modulus and hardness are commonly studied by nanoindentation. Here, a diamond tip is pressed into the specimen and the applied load *P* and corresponding displacement *h* is continuously measured, revealing a load-displacement curve, as schematically depicted in Figure 4.

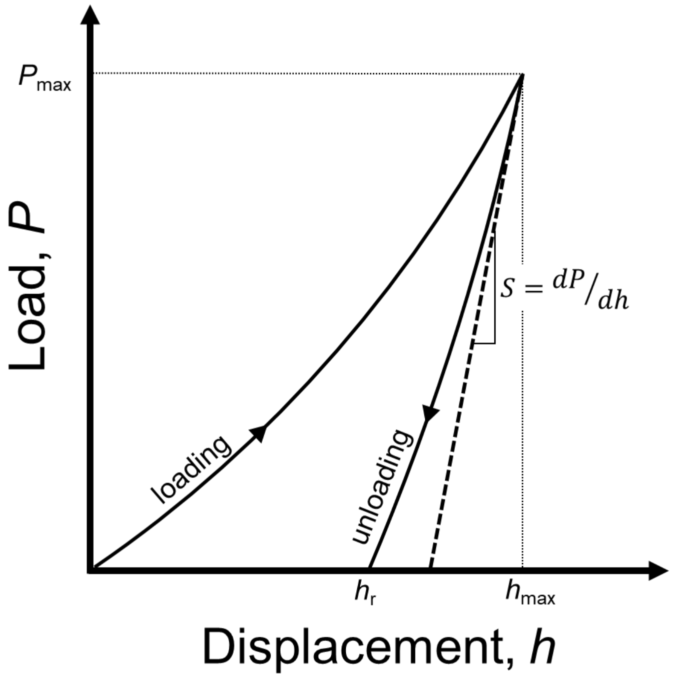

Figure 4: Schematic representation of a load-displacement curve from nanoindentation.

While the loading segment is characterized by both, elastic and plastic deformation, the unloading segment is solely defined by elasticity. Hence, from the slope of the initial part of the unloading segment the stiffness *S* can be quantified. If the contact area A_c

of the diamond tip is known, the reduced elastic modulus E_r [73], which includes the elastic behavior of the specimen and the diamond tip, can be calculated according to:

(4) $$E_r = \frac{\sqrt{\pi}}{2\sqrt{A_c}} \frac{dP}{dh}$$

The reduced elastic modulus can be converted into the elastic modulus of the specimen E_s [73] by

(5) $$\frac{1}{E_r} = \frac{1-\nu_s^2}{E_s} + \frac{1-\nu_i^2}{E_i},$$

where ν_s and ν_i are the Poisson´s ratios of the specimen and diamond tip, respectively. Further information can be found in [74].

2.3. *Ab initio* calculations

Density functional theory is a quantum mechanical *ab initio* modelling method to investigate the electronic structure of a system by approximating a solution for the time-independent Schrödinger equation

(6) $$H\Psi = E\Psi,$$

where H is the Hamiltonian operator, Ψ is the wave-function, and E is the total energy of the system. Based on the Hohenberg-Kohn theorem, the ground state properties of a many-electron system is uniquely defined by a functional of the electron density that only depends on three spatial coordinates, instead of, as for a many-body problem with N electrons, on 3N spatial coordinates [75]. Thus, DFT yields a computationally efficient way to study electronic structures and ground state properties of relatively large (< 500 atoms) and complex systems.

Mechanical properties:

To determine ground-state mechanical properties such as bulk modulus (*B*), elastic modulus (*E*), shear modulus (*G*), or Poisson´s ratio (ν) for cubic systems, first, the equilibrium volume needs to be obtained by fitting energy-volume data using the Birch-Murnaghan equation of state [76]. Secondly, the shear elastic constants (C_{11}-C_{12})/2 and C_{44} can be determined using the following volume conserving distortions $D(\delta)$ and $D_{44}(\delta)$ [77], respectively.

(7) $$D = \begin{pmatrix} 1+\delta & 0 & 0 \\ 0 & 1-\delta & 0 \\ 0 & 0 & \frac{1}{1-\delta^2} \end{pmatrix}$$

(8) $$D_{44} = \begin{pmatrix} 1 & \delta_{44} & 0 \\ \delta_{44} & 1 & 0 \\ 0 & 0 & \frac{1}{1-\delta_{44}^2} \end{pmatrix}$$

The distortion-induced total energy changes are given by

(9) $\Delta E = V(C_{11} - C_{12})\delta^2 + O(\delta^4)$ and

(10) $\Delta E_{44} = 2VC_{44}\delta_{44}^2 + O(\delta_{44}^4)$,

where *V* is the equilibrium volume and δ is the distortion matrix element. Elastic constants are derived from the slope of the linear fit of ΔE vs. δ^2, using equations (9) and (10). An upper and lower bound of *B* and *G* can be derived from the elastic constants C_{ij} and compliance constants s_{ij} by applying the method introduced by Voigt [78] for the upper bound, which assumes a uniform strain throughout the sample, or by the method introduced by Reuss [79] for the lower bound which assumes a uniform stress in the sample:

(11) $B_V = \frac{1}{3}(C_{11}) + \frac{2}{3}(C_{12})$

(12) $G_V = \frac{1}{5}(C_{11} - C_{12}) + \frac{3}{5}C_{44}$

(13) $$B_R = \frac{1}{3s_{11}+6s_{12}}$$

(14) $$G_R = \frac{15}{4s_{11}-4s_{12}+3s_{44}}$$

Hill suggested to utilize the arithmetic average of Voigt and Reuss to calculate the elastic properties, which are called Voigt-Reuss-Hill values [80]:

(15) $$B_{VRH} = \frac{1}{2}(B_V + B_R)$$

(16) $$G_{VRH} = \frac{1}{2}(G_V + G_R)$$

Finally, elastic (Young´s) modulus E and Poisson´s ratio ν are given by

(17) $$E = \frac{9B_{VRH}G_{VRH}}{3B_{VRH}+G_{VRH}}$$

(18) $$\nu = \frac{3B_{VRH}-2G_{VRH}}{2(3B_{VRH}+G_{VRH})}.$$

<u>The Debye-Grüneisen model:</u>

To determine the bulk modulus as a function of temperature, the Debye-Grüneisen model [45, 81] can be used, which accounts for the acoustic phonon vibrational energy. Here, the Helmholtz free energy (F) can be expressed as

(19) $$F = E_0 - Nk_BT\left[3\left(\frac{T}{D}\right)^3\int_0^{\frac{D}{T}}\frac{x^3}{e^x-1}dx - 3\ln\left(1-e^{-\frac{D}{T}}\right) - \frac{9D}{8T}\right],$$

where E_0, N, k_B, T, and D refer to the total energy obtain from the DFT calculations at ground state, number of atoms in the cell, the Boltzmann constant, temperature, and the Debye temperature, respectively. By fitting the free energy – volume data at each temperature using the Birch–Murnaghan equation of state [76], the temperature-dependent bulk modulus is obtained.

3. HPPMS deposition from composite targets: Effect of two orders of magnitude target power density changes on the composition of sputtered Cr-Al-C thin films

3.1. Motivation

Severe compositional deviations (>10 at.%) between compound or composite targets and DCMS deposited thin films have been reported in literature [3-5, 7-15, 17-28], while the effect of HPPMS on compositional deviations has yet not been systematically studied. Therefore, it is meaningful to determine the magnitude of the film – target – composition deviation and to identify the underlying physical mechanisms. In the present study, a Cr-Al-C powder metallurgically fabricated composite target is utilized for thin film growth by DCMS and HPPMS, as it possesses constituents with significantly different masses and binding energies. The effect of target power density, substrate bias potential and substrate temperature on the magnitude of the film – target – composition deviation is investigated systematically.

3.2. Experimental details

The Cr-Al-C thin films were synthesized by magnetron sputtering in an industrial scale PVD system (CemeCon CC 800/9). A powder metallurgically fabricated Cr-Al-C composite target (Plansee Composite Materials GmbH) having a composition of 49.8 at.% Cr, 26.9 at.% Al and 23.3 at.% C was used. The deposition parameters are presented in Table 1. The target peak power density was varied from 2.3 W/cm² (~4.6 W/cm² with respect to race track area) for DCMS to 373 W/cm² (~746 W/cm² with respect to race track area) for HPPMS. A substrate bias potential ranging from floating to -400 V was either applied constantly for DCMS or in synchronized pulses of 200 µs length during HPPMS. The longer pulse length of the substrate bias compared to the target on-time was chosen in order to ensure that the bias is still applied during the afterglow. Si (100) substrates with a 1 µm thick TiN diffusion barrier were either heated to 560 °C prior to deposition or were neither heated nor cooled (RT).

Table 1: Deposition parameters utilized in the industrial CemeCon deposition system.

Deposition parameter	Value
Base pressure	< 6 x 10^{-7} mbar
Ar pressure	3.6 x 10^{-3} – 3.9 x 10^{-3} mbar
Substrate	Si (100) with a 1 µm thick TiN diffusion barrier
Target – substrate distance	7.5 cm
Substrate temperature	Room temperature or 560 °C
Substrate bias potential	Floating, -100 V, -200 V or -400 V
Power supply:	Melec SIPP2000USB-10-500-S
Time-averaged power density	2.3 W/cm²
Peak power density	373 W/cm² and 2.3 W/cm²
Pulse on-time	50 µs (HPPMS) or 4000 µs (DCMS)
Pulse period	4000 µs

Plasma chemistry and energetics were investigated in a lab-scale magnetron sputtering system operating at an Ar partial pressure of 6.5 x 10^{-3} mbar. The base pressure was below 4 x 10^{-8} mbar. A 2 inch powder metallurgically fabricated Cr-Al-C composite target (Plansee Composite Materials GmbH) was installed approximately 7 cm away from the mass-energy analyzer (PPM 422, Pfeiffer Vacuum). The pulse period was increased to 4500 µs while the pulse on-times was kept at 50 µs, in order to obtain target peak power densities of 3.3 W/cm² for DCMS and 361 W/cm² for HPPMS. The target peak power densities are thus comparable to the depositions carried out in the industrial chamber.

Chemical composition data was obtained by ToF-ERDA using 127I ions with an acceleration voltage of 36 MeV. Four samples (DCMS at -400 V bias and 560 °C, HPPMS at -100 V and RT, HPPMS at -400 V and RT, HPPMS at -400 V and 560 °C) were analyzed using a JEOL JSM-6480 scanning electron microscope (SEM) with an EDAX Genesis 2000 EDX device, utilizing an acceleration voltage of 12 kV and a Cr-Al-C thin film sample quantified by ToF-ERDA as a standard. The target composition was measured in a Bruker S8 TIGER Series 2 wavelength dispersive X-ray fluorescence spectrometer.

3.3. Results and discussion

Impurity incorporation from residual gas [82] in the analyzed films resulted in 2 at.% for oxygen, 0.3 at.% for hydrogen and 0.3 at.% for nitrogen. The chemical composition data is shown in Figure 5 for DCMS (2.3 W/cm²) and HPPMS (373 W/cm²) as a function of applied substrate bias potential for RT and 560 °C substrate temperature.

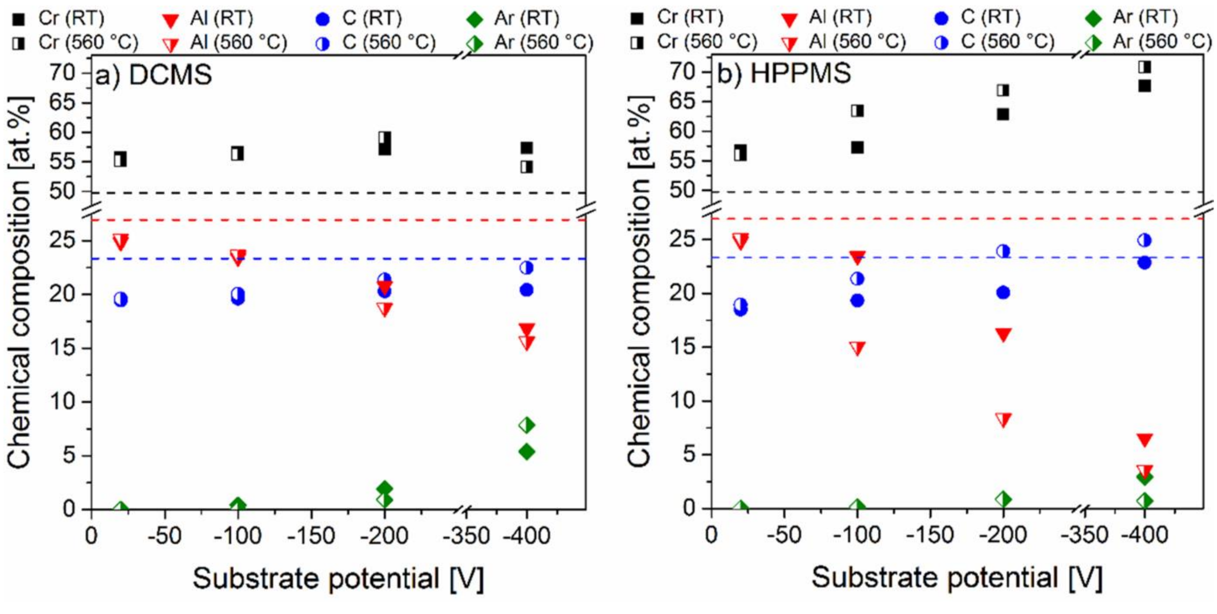

Figure 5: Chemical composition of the Cr-Al-C films as a function of substrate bias potential and temperature for (a) DCMS (2.3 W/cm²) and (b) HPPMS (373 W/cm²). The dashed lines indicate the target composition of 49.8 at.% Cr, 26.9 at.% Al and 23.3 at.% C.

The DCMS deposition (Figure 5 a) carried out at RT and floating potential exhibits a composition of 55.7 at.% Cr, 24.9 at.% Al and 19.4 at.% C. Compared to the target composition, a Cr enrichment (+5.9 at.%) and an Al (-2.0 at.%) and C (-3.9 at.%) deficiency is present. As the substrate bias potential is increased from floating up to -400 V, a pronounced Al depletion of up to 10.1 at.%, i.e. by a factor of 1.6, can be observed together with significant Ar implantation of up to 5.4 at.%. The Cr/C ratio remains approximately constant, indicating that the Al loss is compensated by an increase in both, Cr and C content. The HPPMS depositions carried out at a floating substrate potential and RT reveals nearly the same film composition as for DCMS. However, increasing the substrate bias potential up to -400 V results in even higher Al depletion of up to 20.4 at.%, i.e. by a factor of 4.1, while the amount of incorporated Ar is approximately 50 % lower compared to DCMS. Again, the Al loss is compensated by an increase in both, Cr and C content, as the Cr/C ratios remain approximately constant. As the Al content is strongly substrate bias potential dependent and the applied substrate bias potential controls the energy of film bombarding ions, the plasma chemistry and energetics for the two different process techniques (DCMS and HPPMS) were investigated.

Figure 6 shows total time-averaged energy fluxes towards the growing Cr-Al-C thin films (a) and normalized time-averaged energy fluxes of the gaseous and target-based ions (b) for DCMS and HPPMS.

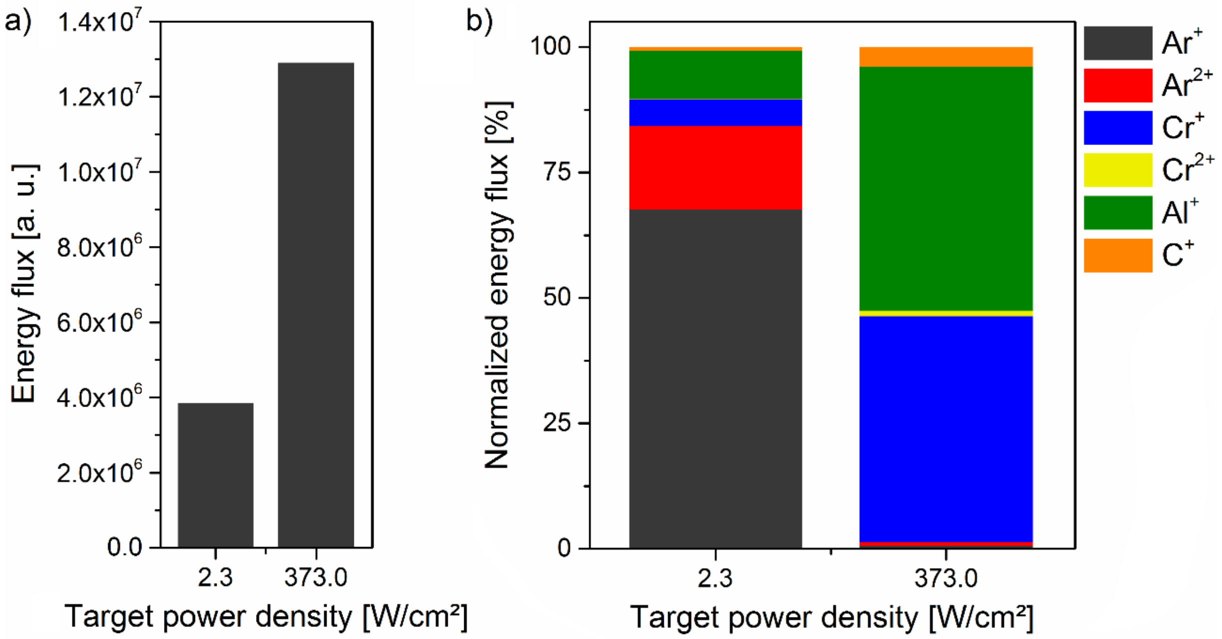

Figure 6: Total time-averaged energy flux towards the growing Cr-Al-C thin film (a) and normalized time-averaged energy fluxes of the gaseous and target-based ions (b) as a function of the target power density.

The energy fluxes related to the gaseous Ar^+ and Ar^{2+} as well as the target-based Cr^+, Cr^{2+}, Al^+ and C^+ ions were calculated as $\text{energy flux} = \int\left(\text{E x IEDF(E)}\right)\text{dE}$, where *E* is the ion energy and the *IEDF* is the ion energy distribution function. Results indicate, that in case of DCMS the energy flux is carried by 67.7 % Ar^+, 16.6 % Ar^{2+}, 9.5 % Al^+, 5.3 % Cr^+, and 0.9 % C^+ (Figure 6 b). Hence, the total energy flux towards the growing thin film is dominated by Ar^+/Ar^{2+} ions for DCMS. The observed increasing Al depletion from 2.0 at.% to 10.1 at.% together with the increasing Ar implantation from 0 at.% to 5.4 at.% for substrate bias potentials of floating to -400 V, respectively, suggests that the Al deficiency is caused by Ar^+/Ar^{2+} ion bombardment. Ar^+ and Ar^{2+} ions are accelerated up to 400 eV and 800 eV, respectively, across the plasma sheath, which increases the probability for Ar implantation, as shown by Winters et al. [83] and provide the required energy to trigger preferential re-sputtering of Al compared to Cr and C. Several reasons can be pointed out emphasizing preferential re-sputtering of

Al compared to Cr and C. Firstly, Al exhibits lower surface binding energies (SBE) [4] (Al-Al: 3.36 eV, Cr-Al: 4.047 eV and Al-C: 5.692 eV) than Cr (Cr-Cr: 4.12 eV and Cr-C: 6.072 eV) and C (C-C: 7.41 eV). Secondly, the efficiency of energy transfer in an elastic collision [84] between film bombarding ions (Ar^+ and Ar^{2+}) and Al or Cr is nearly 1, whereas C exhibits a significantly smaller energy transfer coefficient of 0.7. Thirdly, re-sputtering of Al compared to Cr might be enhanced by the sputter yield amplification effect [85], as Cr possesses twice the mass of Al and hence favors the emission of Al in an elastic collision cascade.

In contrast to DCMS, the major energy flux towards the growing thin film for the HPPMS deposition is mainly carried by target-based Al^+ and Cr^+ ions, as the energy flux (Figure 6 b) consists of 0.7 % Ar^+, 0.7 % Ar^{2+}, 48.6 % Al^+, 45.0 % Cr^+, 1.1 % Cr^{2+}, and 3.9 % C^+. Furthermore, a factor 3.4 higher energy flux is obtained compared to DCMS (Figure 6 a), where the second most frequent target constituent Al is providing the major energy input into the growing film. This may be rationalized by comparing the ionization potentials of the different target constituents. Al exhibits the lowest first ionization potential of 5.99 eV compared to Cr with 6.77 eV and C with 11.3 eV [86], and hence possesses a higher probability of being ionized due to electron impact in the plasma dense region in front of the target. The same trend was observed for V-Al-C [23]. The existence of negligible fractions of doubly charged target-based ions can be attributed to the significantly higher second ionization potentials of Cr (23.3 eV) and Al (24.8 eV) compared to the first ionization potential of Ar (15.8 eV) [86, 87]. The enhanced Al depletion of up to a factor of 4.1 for HPPMS compared to a factor of 1.6 for DCMS might be attributed to the observed changes in the time-averaged energy flux, which is 3.4 times larger for HPPMS and is mainly carried by Al- and Cr-ions instead of Ar-ions. As the observed Al deficiency for DCMS is suggested to stem from preferential re-sputtering of Al triggered by Ar-ion bombardment, the change to an approximately 50 % Al-ion carried time-averaged energy flux for HPPMS might enhance the preferential re-sputtering of Al due to self-(re-)sputtering. Furthermore, by additionally considering the time-characteristic during the HPPMS deposition, where the growing film is temporarily exposed to immense ion bombardment and hence to an immense energy flux, the preferential re-sputtering of Al might be further enhanced. To illustrate this, the substrate current densities for DCMS and HPPMS at -400 V substrate bias potential were measured and are depicted in Figure 7.

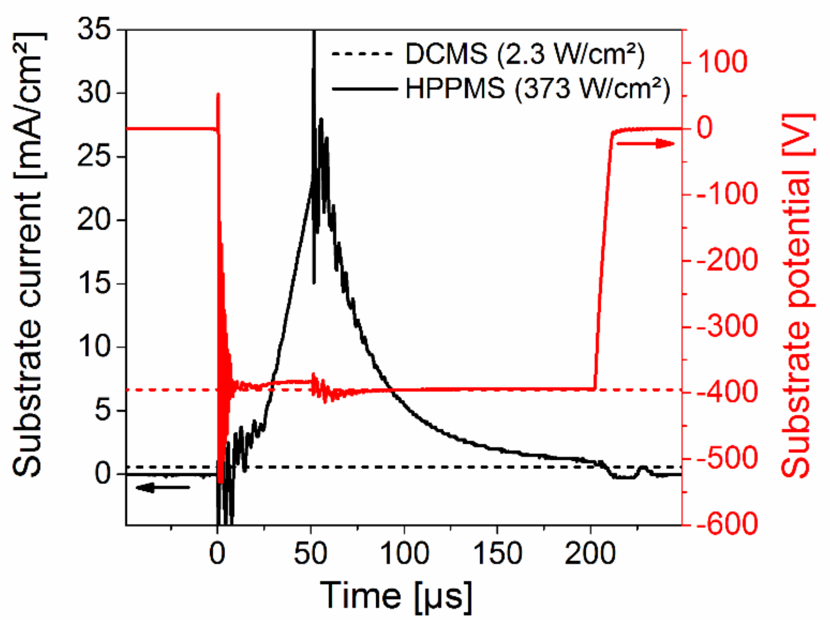

Figure 7: Substrate current densities (black) and voltages (red) for DCMS (dashed) and HPPMS (solid) at -400 V substrate bias potential.

The instantaneous flux of the positive ions bombarding the film can be estimated from the substrate current density, if the emission of secondary electrons from the substrate is neglected and only single charged ions are assumed to be present. This is a valid assumption, as less than 2 % of the time-averaged energy flux is carried by double charged ions in case of HPPMS (see Figure 6 b). For HPPMS, the maximum flux of instantaneously film bombarding ions can be estimated to be 1.6×10^{11} ions/ ($cm^2 \times \mu s$), whereas a rough estimation (due to the presence of Ar^{2+} ions) for DCMS deposition is 3.5×10^{9} ions/ ($cm^2 \times \mu s$). Nevertheless, the number of simultaneously film bombarding ions is roughly 50 times larger for HPPMS (as compared to DCMS), which significantly increases the dissipated energy per area and per time and thus might favor the preferential re-sputtering of Al. This, together with the factor 3.4 larger time-averaged energy flux and the occurrence of Al self-(re-)sputtering might cause the observed 10.3 at.% increase in the Al deficiency from 10.1at.% for DCMS to 20.4 at.% for HPPMS.

The effect of target power density on the composition at elevated temperatures (Figure 5) was investigated by additionally depositing films at 560 °C substrate temperature (prior to deposition). At floating potential, similar compositions are observed for both DCMS and HPPMS compared to the respective RT depositions and similar substrate temperature increases during deposition (ΔT_S) of 3-4 K are obtained. As the substrate bias potential is increased to -200 V and -400 V for the DCMS depositions, an increase in the Al deficiency compared to RT depositions of 2.6 at.% and 1.3 at.%, respectively, together with an increase in ΔT_S of 10 K and 13 K is observed. Utilizing HPPMS reveals enhanced Al deficiencies compared to RT depositions already at -100 V substrate bias potential of 8.6 at.% together with an increase in ΔT_S of 13 K. As the substrate bias potential is further increased to -200 V and -400 V, Al deficiencies compared to RT deposition by an additional factor of 1.9 together with an increase in ΔT_S of 16 K and 32 K, respectively are obtained. The observed increase in ΔT_S most probably stems from atomic scale heating [86], which mainly originates from the kinetic and potential energy of the ion flux. As this energy is dissipated at the surface or in the surface near volume of the growing thin film, the surface temperature might exceed the measured substrate temperature and hence cause the observed additional Al deficiency compared to RT depositions by thermal desorption of Al, as e.g. observed for the growth of Ti_2AlC [14]. The enhanced Al deficiency of 8.6 at.% for HPPMS compared to 2.6 at.% for DCMS at a substrate bias potential of -200 V might be attributed to the 6 K larger increase in ΔT_S possibly stemming from the 3.4 times larger time-averaged energy flux and to the occurrence of periodic atomic scale heating, as the required film bombarding ions are mainly present during a short time period (Figure 7) and hence it can be assumed that the ΔT_S during this time period exceeds the measured time-averaged ΔT_S of 6 K thus enhancing the thermal desorption of Al.

4. Effect of target power density on the phase formation, microstructure evolution and mechanical properties of Cr_2AlC MAX-phase coatings

4.1. Motivation

To utilize Cr_2AlC as protective coatings in nuclear or aerospace applications, several processing related requirements need to be fulfilled: The deposition of single-phase and dense coatings, the homogeneous deposition over large areas, and the deposition at low substrate temperatures. To hollistically adress these requirements, the utilization of composite or compound targets in combination with ion-assisted growth is needed, even though, as discussed in chapter 3, compositional deviations between target and thin film can be expected. Therefore, the phase formation, microstructure evolution and mechanical properties of Cr_2AlC are studied utilizing DCMS and HPPMS as a function of applied substrate bias. To compensate the expected target power density and substrate bias induced Al-deficiencies, a split $Cr_{0.46}$-$Al_{0.25}$-$C_{0.29}$/$Cr_{0.15}$-$Al_{0.75}$-$C_{0.10}$ composite target approach, according to the design concept of Shang *et al.* [88], is applied.

4.2. Experimental details

The Cr-Al-C thin films were synthesized by combinatorial magnetron sputtering [88] in an industrial scale PVD system (CemeCon CC 800/9). A powder metallurgically fabricated split $Cr_{0.46}$-$Al_{0.25}$-$C_{0.29}$ / $Cr_{0.15}$-$Al_{0.75}$-$C_{0.10}$ composite target (Plansee Composite Materials GmbH) with a size of 500 × 88 mm² was used. Several cemented carbide substrates were mounted at a target-to-substrate distance of 75 mm along the aluminium target gradient and were heated to 560 °C prior to deposition. The base pressure for all depositions was below 0.6 mPa and the gas flow during deposition was 200 sccm Ar, resulting in a deposition pressure of 0.39 Pa. Two Melec HPPMS generators (SIPP2000USB-10-500-S) for powering the target and applying the substrate bias were used. The target peak power density was varied from 2.3 W/cm^2 for DCMS to approximatelly 460 W/cm^2 for HPPMS, which was achieved by utilizing a frequency of 250 Hz, a duty cycle of 1.25%, and a time-average power of 1000 W. A substrate bias potential ranging from floating to -400 V was either applied constantly for DCMS or in synchronized pulses of 200 µs length during HPPMS. The longer pulse length of the substrate bias compared to the target on-time was chosen in order to ensure that the bias is still applied during the afterglow.

Chemical composition data was obtained using a JEOL JSM-6480 scanning electron microscope (SEM) with an EDAX Genesis 2000 energy dispersive X-ray spectroscopy device, utilizing an acceleration voltage of 12 kV with a Cr_2AlC thin-film sample (Cr: 49.9 ± 2.5 at.%, Al 24.9 ± 1.2 at.%, C: 24.7 ± 1.2 at.% and O: 0.5 ± 0.3 at.%) [89] quantified by elastic backscattering spectroscopy (EBS) as a standard.

Out-of plane X-ray diffraction (XRD) analysis of the deposited thin films was carried out with a Siemens D5000 system equipped with a Cu radiation source operating at a voltage and current of 40 kV and 40 mA, respectively. The diffractometer was operated in Bragg-Brentano mode using a step size of 0.02° and a scan time of 1 s per step. In-plane XRD analysis was performed with a Rigaku Ultima IV diffractometer using Cu radiation (source parameters: 40 kV, 40 mA). Mandatory for in-plane diffractometry, the system was operated in parallel beam geometry in order to accurately set a small incidence angle of < 0.3° with respect to the sample surface at a small beam divergence. Primary and secondary 2.5° parallel slit collimators were inserted as angular resolution defining elements. Using the in-plane detector arm axis $2\theta_\chi$ of the instrument, $2\theta_\chi/\varphi$ diffractograms were measured with a step size of 0.1° and a scan speed of 0.5°/min. Furthermore, structural characterization of the thin films by selected area electron diffraction (SAED) and scanning electron nanobeam diffraction (SEND) was conducted using a 200 kV Tecnai F20 transmission electron microscope (TEM) retrofitted with an ASTAR-system (NanoMEGAS SPRL, Brussels, Belgium). SEND dataset analysis was carried out with the software package ACOM-TEM [90-92] and structural drawings were performed with the program VESTA3 [93]. Cross-sectional TEM lamellae were prepared using a standard lift-out method in a DualBeam focused ion beam (FIB) system (Helios NanoLab 660). A thin layer of Pt was deposited on the film surface for protection against the beam damage. Ar ion milling was applied to remove amorphous and implanted layers on TEM lamellae prepared by FIB.

Nanoindentation was carried out in a Hysitron TI-900 TriboIndenter and Young´s modulus of each film was determined by the Oliver–Pharr method [73]. A Berkovich diamond tip was used in load-controlled mode and the maximum force of 8 mN resulted in a contact depth of < 10% of the coating thickness. A minimum of 72 indentation experiments was carried out for each sample, and the tip area function was determined with a fused silica standard. A Poisson's ratio (ν) of 0.236 [94] was used for Cr_2AlC and for $(Cr,Al)_2C_x$.

4.3. Computational details

Ab initio calculations were carried out using density functional theory (DFT) [95] as implemented in the Vienna *Ab Initio* Simulation Package (VASP) [96, 97] wherein projector augmented wave potentials [98] were employed. The generalized-gradient approximation, as introduced by Perdew, Burke and Ernzerhof [99], a convergence criterion for relaxation of 0.01 meV and Blöchl corrections for the total energy cut-off [100] of 500 eV were applied. Brillouin zone integration was carried out with a 7 × 7 × 3 and 5 × 5 × 3 Monkhorst–Pack k-point mesh [101] for Cr_2AlC and $(Cr,Al)_2C_x$, respectively. A 3 × 3 × 2 supercell with 144 atoms was utilized for Cr_2AlC and a supercell with 64 atoms according to the work of Abdulkadhim, et al. [102] was used for $(Cr,Al)_2C_x$. Full structural relaxation was performed for every configuration and the Birch–Murnaghan equation of state [76] was utilized to obtain the bulk moduli. Stress-state and temperature dependent Young´s moduli were determined using the Debye-Grüneisen model [81] as described elsewhere [45, 103] by assuming a Poisson´s ratio (ν) of 0.236 [94] for both, Cr_2AlC and $(Cr,Al)_2C_x$. Data used to directly compare theoretical and experimental elasticity in this work were obtained at 300 K.

4.4. Results and discussion

Composition analysis was conducted by EDX employing an EBS and ERDA quantified standard sample for calibration. One Cr-Al-C thin film from each combinatorial deposition utilizing the split $Cr_{0.46}$-$Al_{0.25}$-$C_{0.29}$ / $Cr_{0.15}$-$Al_{0.75}$-$C_{0.10}$ composite target exhibiting a composition close to the ideal Cr_2AlC composition was selected for this research. The compositions of the selected samples are presented in Table 2.

Table 2: Chemical composition ratios of Cr-Al-C thin films determined by standardized EDX analysis. Errors for Cr/Al and Cr/C ratios are based on the relative error of ± 5 % of the EBS measured standard.

Sputtering mode	**Substrate bias**	**Cr/Al**	**Cr/C**
DCMS	floating	1.81 ± 0.18	1.93 ± 0.19
DCMS	-60 V	1.36 ± 0.14	1.53 ± 0.15
DCMS	-100 V	1.42 ± 0.14	1.60 ± 0.16
DCMS	-200 V	1.71 ± 0.17	1.58 ± 0.16
DCMS	-400 V	1.73 ± 0.17	1.74 ± 0.17
HPPMS	floating	1.56 ± 0.16	1.70 ± 0.17
HPPMS	-60 V	1.97 ± 0.20	1.58 ± 0.16
HPPMS	-100 V	1.52 ± 0.15	1.64 ± 0.16
HPPMS	-200 V	1.37 ± 0.14	1.68 ± 0.17
HPPMS	-400 V	1.54 ± 0.15	1.84 ± 0.18

All coatings, except the DCMS deposited sample at -60 V exhibit Cr/Al and Cr/C ratios within the compositional Cr_2AlC MAX-phase formation range reported by Mertens et al. of Cr/Al = 1.42 – 2.03 and Cr/C = 1.72 – 1.93 [104], if the compositional uncertainty of ± 5% (relative) of the EBS quantified standard is considered. Impurity incorporation from residual gas [82] in the analyzed films results in less than 1 at.% for oxygen. Due to the applied substrate bias, Ar incorporation for DCMS with -200 and -400 V of 1.0 at.% and 5.5 at.%, respectively, and for HPPMS with -200 and -400 V of 0.7 at.% and 2.3 at.%, respectively, were obtained by EDX.

Diffractograms of Cr-Al-C coatings synthesized by DCMS and HPPMS as a function of applied substrate bias on cemented carbide substrates are presented in Figure 8.

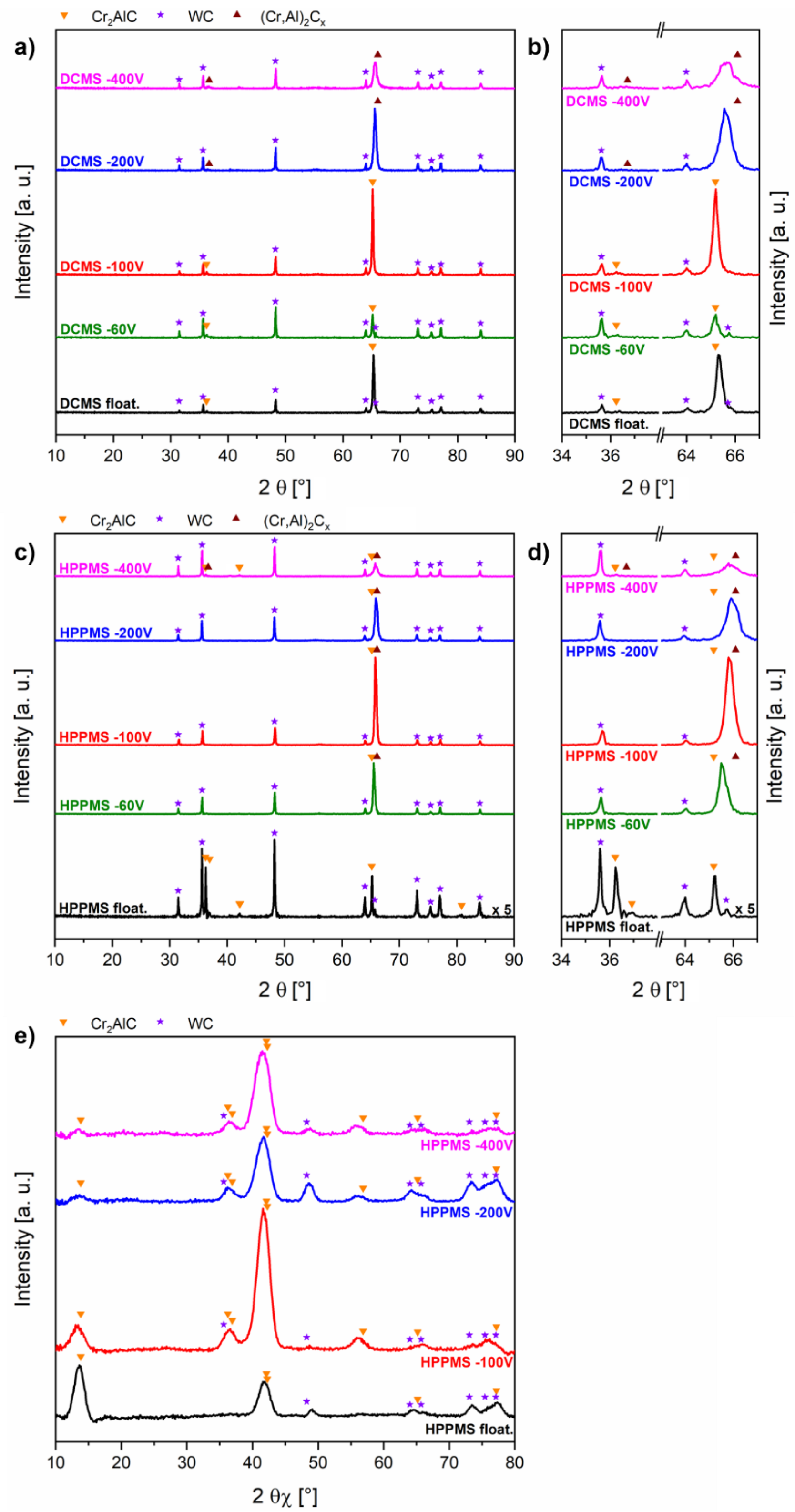

Figure 8: X-ray diffractograms of Cr-Al-C thin films grown by DCMS (a and b) and HPPMS (c and d) as a function of applied substrate bias with close-ups of the (100) peak at 2θ = 36.236° [105], the, (101) peak at 2θ = 36.930° [105] and the (110) peak at 2θ = 65.185° [105] (b and d). In-plane XRD measurements of Cr-Al-C thin films grown by HPPMS as a function of applied substrate bias e).

For DCMS (Figure 8 a and b) strongly (110) oriented thin films are obtained. Due to the preferred (110) orientation, a clear distinction between the MAX-phase Cr_2AlC and the structurally similar hexagonal disordered solid solution $(Cr,Al)_2C_x$ based on XRD alone is not feasible, as distinct indicators for the MAX-phase formation, such as the (002) basal plane peak at 13.8° or the (101) peak at 36.9° are not observed. Additionally, the (110) texture prevents a conclusive residual stress analysis by XRD. To verify the Cr_2AlC MAX-phase formation, cross-sectional SAED analysis was performed on FIB cross-sections (Figure 9). For DCMS grown samples at floating and -100 V substrate bias, the (002) basal plane reflection of Cr_2AlC was detected, indicating the formation of Cr_2AlC MAX-phase. Decreasing the substrate bias further to -200 V results in the disappearance of the (002) basal plane diffraction spots in the analyzed area of 3 µm² (Figure 9 c), suggesting a phase formation change from Cr_2AlC to the disordered solid solution $(Cr,Al)_2C_x$. This is in line with the observation of a significant (110) peak shift in obtained diffractograms (Figure 8 b) for the DCMS deposited samples at -200 and -400 V compared to samples deposited at floating, -60, and -100 V towards higher 2θ values. This is consistent with the formation of $(Cr,Al)_2C_x$ as the disordered solid solution exhibits a smaller *a*-lattice parameter compared to Cr_2AlC [102]. Ion bombardment induced compressive stress would cause a peak shift towards lower 2θ values. This phase formation change along with peak broadening of the (110) peak, indicating smaller domain sizes, for samples deposited at -200 and -400 V may result from high-energy Ar-ion bombardment, which is consistent with the enhanced Ar incorporation of 1.0 at.% and 5.5 at.% for -200 and -400 V, respectively. High-energy Ar-ion bombardment during film growth appears to cause detrimental effects for the formation of the complex Cr_2AlC structure [1] leading to the formation of the disordered solid solution. While too high energies of film bombarding

Ar-ions are detrimental for the formation of Cr_2AlC, too low energies result in an unfavorable microstructure, as can be seen in the TEM image in Figure 9 a). The microstructure of the Cr_2AlC coating deposited at floating potential is characterized by a coarse-grained columnar microstructure with partially under-dense column boundaries stemming from insufficient adatom mobility. As the substrate bias potential is decreased and hence the energy of film bombarding Ar-ions is increased, a fine-grained microstructures with dense column boundaries is obtained at -100 and -200 V substrate bias (see Figure 9 b and c), indicating Ar-ion bombardment induced densification as well as disruption of grain growth resulting in renucleation [106]. This results in smaller domain sizes. Hence, a substrate bias potential smaller than the floating potential and larger than -200 V seems favorable for the synthesis of Cr_2AlC thin films utilizing DCMS, as too low ion energies result in partially under-dense microstructures, whereas too high ion energies results in the formation of the disordered solid solution $(Cr,Al)_2C_x$ which is accompanied by severe Ar-incorporation of up to 5.5 at.%.

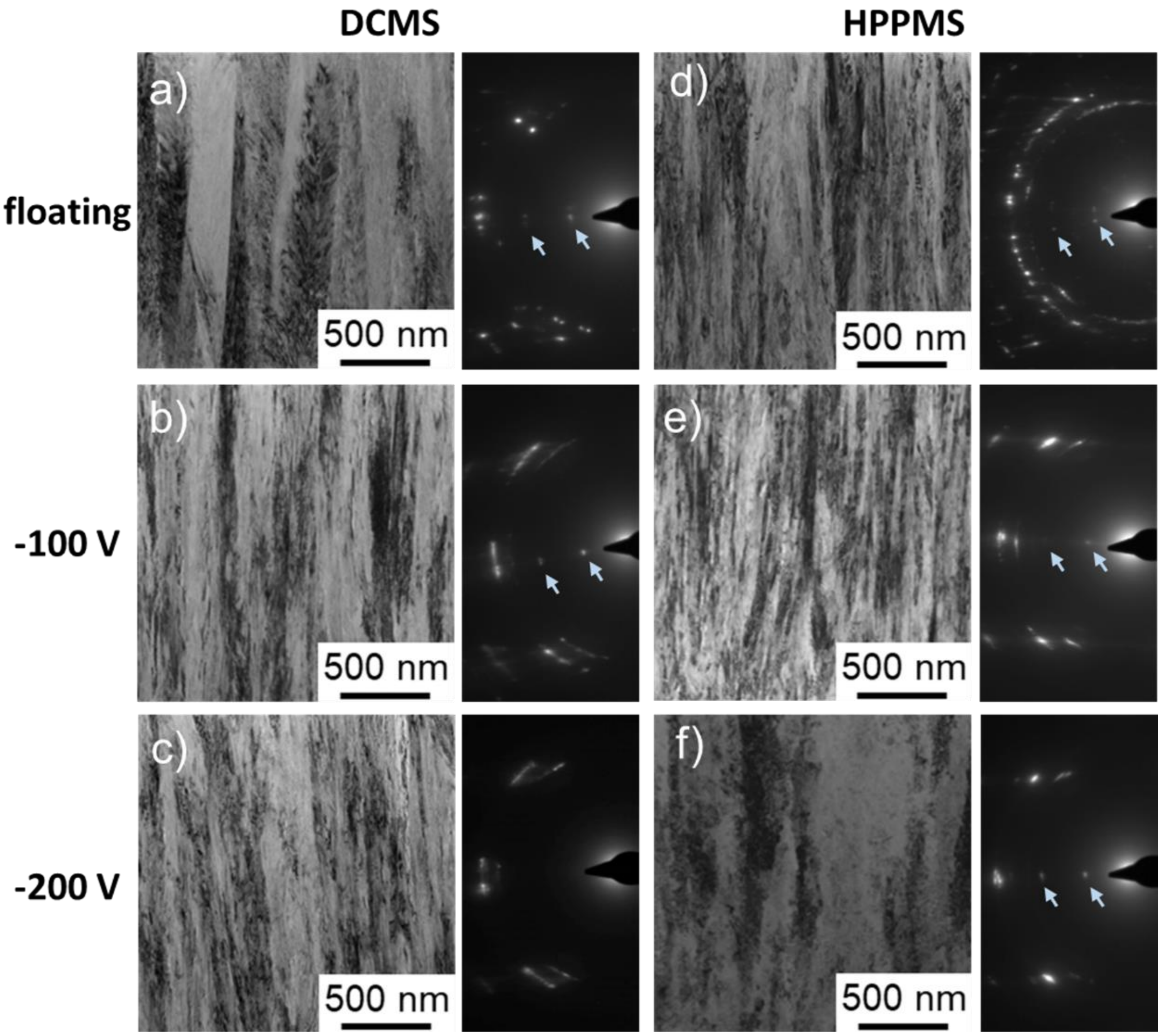

Figure 9: Bright field TEM cross sections and SAED patterns of DCMS floating (a), -100 V (b), and -200 V (c) as well as of HPPMS floating (d), -100 V (e), and -200 V (f) deposited samples. Highlighted diffraction signals (arrows) index the (002) and (004) plane reflexes of Cr_2AlC.

The HPPMS deposited sample at floating potential exhibits a preferred (100) and (110) orientation (Figure 8 c and d) and hence, due to the present texture the characteristic (002) basal plane peak of Cr_2AlC cannot be observed. An in-plane XRD measurement (Figure 8 e) carried out on the HPPMS deposited sample at floating potential as well as the SAED pattern obtained on a cross-section lamella (Figure 9 d) reveal the (002) basal plane peak, which again indicates the formation of Cr_2AlC. While the phase formation seems to be similar to the DCMS deposition at floating potential, the obtained microstructure appears to be fine-grained with dense column boundaries instead of coarse-grained with partially under-dense column boundaries as observed for DCMS. This change may be attributed to a higher adatom mobility during thin film growth for the HPPMS deposition, which results from a higher time-averaged energy flux in combination with large fractions of ionized film-forming species which are present in the HPPMS plasma [107]. Decreasing the substrate bias potential down to -400 V results on the one hand in a preferred (110) orientation of the deposited thin films and on the other hand in a continuous peak shift of the (110) peak towards higher 2θ values (Figure 8 c and d). SAED results (Figure 9 e and f) obtained for an area of approximately 3 µm^2 as well as in-plane XRD measurements (Figure 8 e) indicate the presence of Cr_2AlC for -100 and -200 V due to clear diffraction spots of the (002) and (004) basal planes and the presence of the (002) basal plane peak, respectively. However, the possible concurrent formation of the disordered solid solution cannot be excluded due to the preferred growth and thus inhibits an estimation of the amount of Cr_2AlC and $(Cr,Al)_2C_x$. Thus, an in detail analysis of the growth characteristics of the three HPPMS samples grown at floating, -100, and -200 V by conventional TEM, SAED, and SEND utilizing the ACOM-TEM software package was performed (for details see Figures S1-S3 in the Appendix). Based on these investigations, d_{110} values were extracted and are depicted together with d_{110} spacings obtained from XRD in Figure 10. Decreasing $d_{110}/d_{110,floating}$ ratios for decreasing substrate bias can be observed, which allows to estimate the phase content trends of Cr_2AlC and $(Cr,Al)_2C_x$, since the 110 Laue diffraction is unaffected by the degree of structural ordering/disordering along the *c*-axis. The decreasing $d_{110}/d_{110,floating}$ ratios upon substrate bias voltage decrease implies a significant shrinkage of the *a*-axis of up to

10%, which compared to the DFT predicted change in $\boldsymbol{d_{110,Cr_2AlC}/d_{110,Cr_2AlC}}$ to $\boldsymbol{d_{110,(Cr,Al)_2C_x}/d_{110,Cr_2AlC}}$ ratios of 10% may imply the formation of significant amounts of $(Cr,Al)_2C_x$ at -200 V substrate bias. This indicates that the volume fraction of Cr_2AlC may be controlled by the applied substrate bias voltage during synthesis, i.e. the more negative the applied voltage, the more disordered solid solution is obtained.

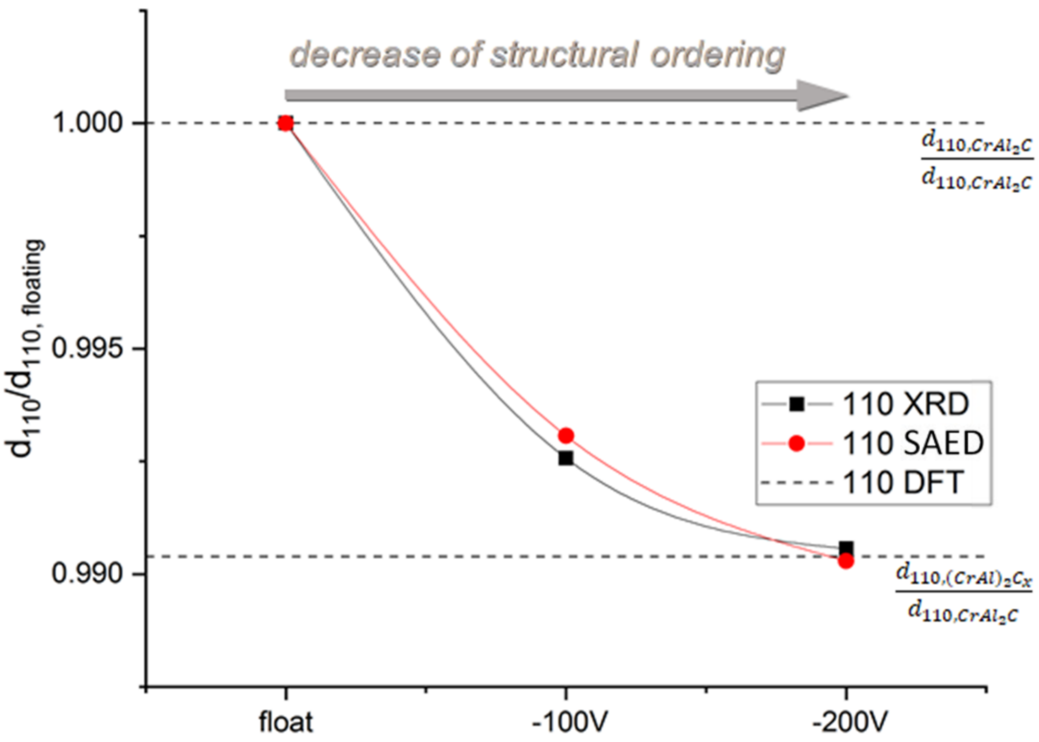

Figure 10: Plot of the normalized relative interplanar spacings of the 110 diffraction spot from selected area electron diffraction (SAED), X-ray diffraction (XRD) of HPPMS deposited samples and density functional theory (DFT) calculation.

The increase in phase fraction of $(Cr,Al)_2C_x$ with decreasing substrate bias may be attributed to detrimental effects for the formation of the complex Cr_2AlC structure due to ion-bombardment [1] causing the formation of the disordered solid solution. However, in contrast to the DCMS depositions, where a sudden phase formation change from Cr_2AlC to the disordered solid solution $(Cr,Al)_2C_x$ between -100 and -200 V substrate bias potential for the analyzed area of 3 μm^2 can be observed, the phase content of $(Cr,Al)_2C_x$ gradually increases with decreasing substrate bias for HPPMS. It is reasonable to assume that this originates from differences in plasma chemistry and energetics. While the DCMS plasma mainly consists of Ar-ions, the HPPMS plasma is characterized by large fractions of film-forming ions and overall larger energy fluxes towards the growing thin film [107]. In combination with an ideal energy transfer function of the ionized film-forming species upon film bombardment in case of HPPMS, the continuous increase of $(Cr,Al)_2C_x$ due to detrimental effects caused by ion-bombardment may be rationalized. Apart from increasing volume fractions of $(Cr,Al)_2C_x$ upon substrate bias decrease, a change in microstructure (Figure 9 d-f) from a fine-grained microstructure with dense column boundaries (Figure 9 d) at floating potential over interrupted grain growth (Figure 9 e) at -100 V substrate bias to a more featureless appearance (Figure 9 f) for -200 V can be observed. Furthermore, peak broadening of the (110) peak (Figure 8 d) with decreasing substrate bias can be observed similar to DCMS. This can be attributed to decreasing grain sizes as revealed by grain size distributions analysis (Figure S4) for floating, -100, and -200 V, resulting from increasing energies of film bombarding ions causing disruption of grain growth, which results in repeated nucleation [106] and thus smaller grain sizes.

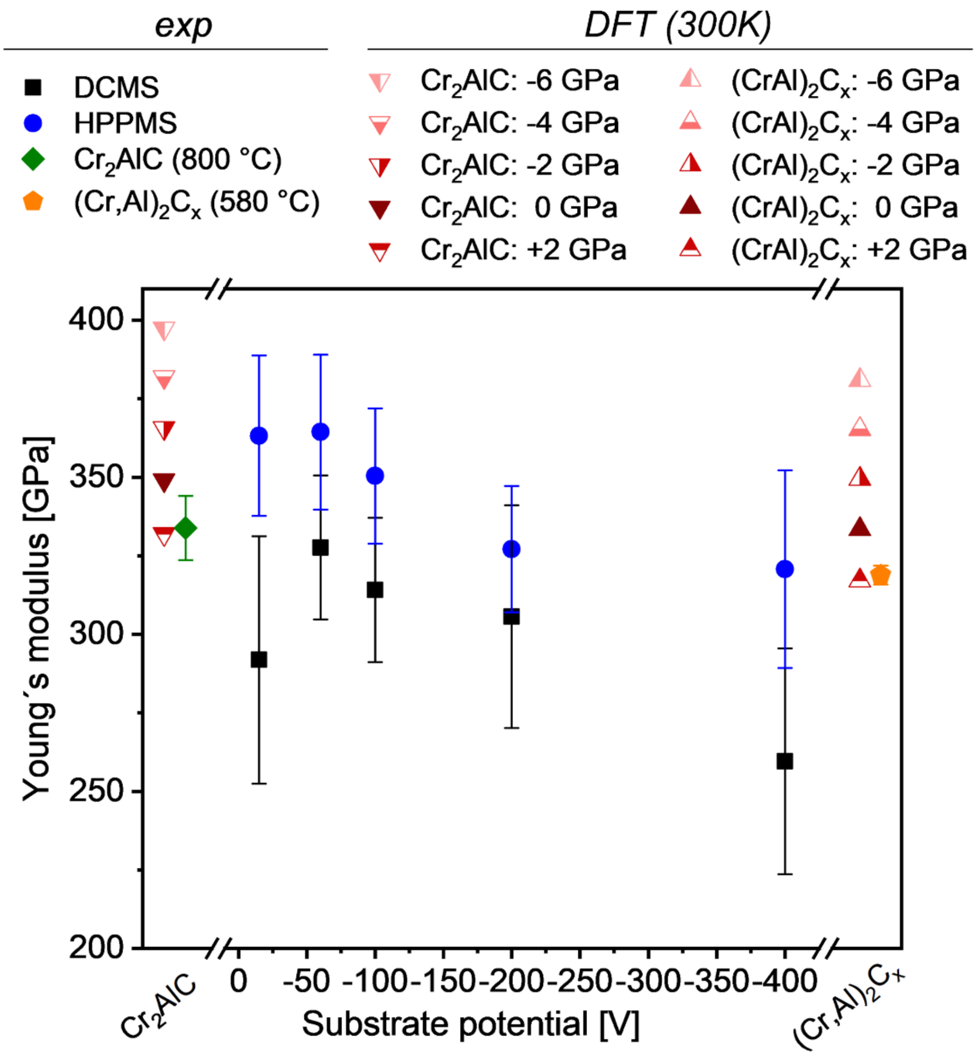

Figure 11: Young´s moduli of Cr_2AlC and $(Cr,Al)_2C_x$ thin films grown by DCMS (squares) and HPPMS (circles) as a function of substrate bias determined by nanoindentation. For comparison, a Cr_2AlC and $(Cr,Al)_2C_x$ sample obtained by annealing amorphous Cr-Al-C films at 800 and 580 °C, respectively, are shown. DFT (300 K) data (triangles) include the stress state dependence for the MAX-phase Cr_2AlC and for the disordered solid solution $(Cr,Al)_2C_x$.

Young's moduli of Cr-Al-C coatings deposited by DCMS and HPPMS were measured by nanoindentation and are presented in Figure 11 as a function of applied substrate bias. The average Young´s moduli for DCMS deposited samples first increase from 292 ± 39 GPa at floating potential to 327 ± 23 GPa at -60 V and then decrease to 260 ± 36 GPa for -400 V substrate bias, while for HPPMS a continuous decrease in Young´s moduli from 363 ± 26 GPa at floating potential to 321 ± 31 GPa at -400 V substrate bias can be observed. For comparison, on the one hand stress state dependent Young´s moduli of Cr_2AlC and $(Cr,Al)_2C_x$ were calculated by DFT at 300 K utilizing the Debye-Grüneisen model. On the other hand, Young´s moduli of Cr_2AlC and $(Cr,Al)_2C_x$ samples, which are obtained by depositing an amorphous Cr-Al-C thin film and subsequently annealing it at 580 or 800 °C, respectively, in order to form samples with dense microstructures and equiaxed grains according to the procedure described elsewhere [89], are depicted in Figure 11. The annealed Cr_2AlC sample possesses a Young´s modulus of 334 ± 10 GPa and the $(Cr,Al)_2C_x$ sample exhibits a Young´s modulus of 319 ± 3 GPa. Both Young´s moduli values are in excellent agreement with the *ab initio* derived Young´s moduli for the stress free scenario of 349 and 333 GPa for Cr_2AlC and $(Cr,Al)_2C_x$, respectively. The Young´s modulus of the DCMS deposited samples at floating potential is 292 ± 39 GPa, which is in excellent agreement with a previously reported Young´s modulus of 298 ± 21 GPa obtained under similar deposition conditions by Schneider et al. [30]. However, it is 11% smaller than the Young´s modulus of the annealed Cr_2AlC sample and 13% smaller than the *ab initio* values, which may be due to porosity [108] induced by the coarse-grained columnar microstructure with partially under-dense column boundaries. The increase and subsequent decrease in Young´s modulus for DCMS deposited sample at -60, -100, -200, and -400 V may be attributed to a complex interplay of Ar-ion bombardment induced effects. While Ar-ion bombardment may cause densification [108] and/or compressive stresses, which according to *ab initio* calculation can increase the Young´s modulus of Cr_2AlC at 300 K from 349 GPa for a stress free scenario to 367, 382, and 397 GPa for compressive stresses of -2, -4, and -6 GPa, respectively, it may also induce detrimental effects. These detrimental effects cause on the one hand the formation of the disordered solid solution $(Cr,Al)_2C_x$, which according to *ab initio* calculation as well as the annealed reference thin film possess a lower Young´s modulus and on the other hand cause severe Ar incorporation of 1.0 at.% and 5.0 at.% for -200 and -400 V substrate bias, respectively. For HPPMS, a Young´s modulus of 363 ± 26 GPa is obtained at floating potential, which is 24% larger than the one of DCMS, 9% larger than the Young´s modulus of the Cr_2AlC sample, and 4 % larger than the *ab initio* value. This may be attributed to the microstructure with dense column boundaries as well as to possible compressive stress states due to the higher energy input during HPPMS. As the substrate bias is decreased to -100, -200 and -400 V, a gradual decrease in Young´s moduli to 350 ± 21, 327 ± 20, and 321 ± 31 GPa, respectively, can be observed. This may again be attributed to a complex interplay of film-forming-ions and Ar-ion bombardment induced effects causing the increasing formation of the less stiff hexagonal disordered solid solution, the Ar incorporation of 0.7 at.% and 2.3 at.% for -200 and -400 V substrate bias, and may affect the residual stress state evolution. Furthermore, some authors have argued that Cr_2AlC exhibits strong correlations effects, which softens the lattice [109, 110]. No evidence for these effects is found in the current work since temperature and stress modulations suffice to obtain consistency between the theoretical and experimental data on elasticity.

5. Effect of chemical composition, defect structure, and stress state on the elastic properties of $(V_{1-x}Al_x)_{1-y}N_y$

5.1. Motivation

For $(V_{1-x}Al_x)_{1-y}N_y$ an extensive and theoretically unexplained spread in experimentally obtained elastic moduli ranging from 254 to 599 GPa and hence 58 % is reported in literature, as depicted in Figure 12.

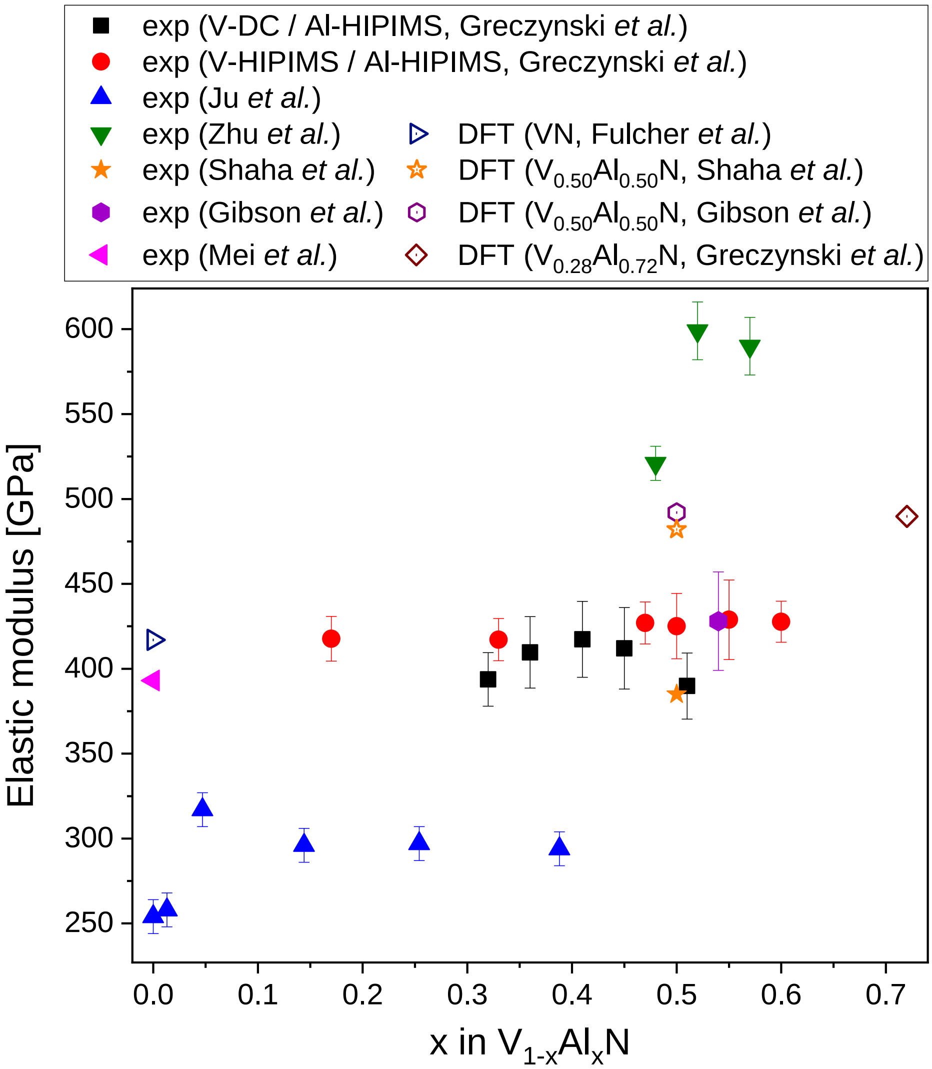

Figure 12: Elastic modulus vs. x in $V_{1-x}Al_xN$ obtained by experiments (Greczynski *et al.* [57], Ju *et al.* [58], Zhu *et al.* [111], Shaha *et al.* [56], Gibson *et al.* [55], and Mei *et al.* [59]) and density functional theory (DFT) calculations (Fulcher *et al.* [112], Shaha *et al.* [56], Gibson *et al.* [55], Greczynski *et al.* [53]). Elastic or indentation moduli from these studies [53, 56, 58, 111] have been recalculated utilizing Poisson´s ratios from Greczynski *et al.* [57] to enable a direct comparison.

Ab initio calculations predict an Al concentration induced increase in elastic modulus of 18 % from 417 GPa for $V_{0.5}N_{0.5}$ [112] to 492 GPa for $(V_{0.5}Al_{0.5})_{0.5}N_{0.5}$ [55]. The experimentally reported increase in this concentration range is with 136 % 7.5 times larger. No explanation for this rather extensive difference can be found in literature. As it can be seen in Figure 12, excellent agreement between the experimentally obtained elastic modulus of 393 GPa for stoichiometric VN with small compressive strains of -0.26 % from Mei *et al.* [59] and the *ab initio* predicted elastic modulus of 417 GPa [112] can be observed, especially if the temperature dependence of the elastic modulus is considered, as the experimental elastic modulus is obtained at room temperature, whereas the *ab initio* derived one is predicted for ground state and hence for 0 K. Comparing the experimentally obtained elastic modulus of 393 GPa for stoichiometric VN from Mei *et al.* [59] with measured elastic moduli of 254 to 258 GPa in the compositional range of $0 \leq x \leq 0.01$ with tensile residual stress states of +2.3 to +1.6 GPa and N/M-ratios between 0.93 and 0.96 from Ju *et al.* [58] yields a difference of 35 %, whereby its cause remains unexplained. For $(V_{1-x}Al_x)_{1-y}N_y$, elastic moduli of 310 to 282 GPa for $0.05 \leq x \leq 0.39$ with residual stress states of +1.2 to -0.8 GPa and N/M-ratios between 0.96 and 0.97 were measured by Ju *et al.*[58]. Greczynski *et al.* reported elastic moduli of 390 to 428 GPa for $0.17 \leq x \leq 0.63$ and residual stress states of 0 and -5 GPa, but no information regarding N/M-ratio was presented [57]. Zhu *et al.* obtained elastic moduli of 530 and 599 GPa for $0.48 \leq x \leq 0.57$, but they neither stated exact N/M-ratios nor residual stress states but assumed compressive stress states to be present due to an applied substrate bias of -90 V [111]. As most data sets lack either information on the stress states or N/M-ratios, a comparison between them or with *ab initio* derived elastic moduli, which are reported to be in the range of E = 417 – 492 GPa [55, 56, 112] and thus are up to 20 % smaller or up to 40 % larger

(Figure 12), does not reveal the cause for the extensive reported elastic modulus spread. To identify the origin of the observed elastic modulus spread in the literature for $(V_{1-x}Al_x)_{1-y}N_y$, we carry out a systematic *ab initio* study of the effects of the Al concentration (x), N/M-ratio (y), and stress state on the elastic modulus of $(V_{1-x}Al_x)_{1-y}N_y$ at room temperature to reveal the underlying causalities.

5.2. Computational details

Ab initio calculations are carried out using density functional theory (DFT) [95] as implemented in the Vienna *ab initio* simulation package (VASP) [96, 97] wherein projector augmented wave potentials [98] are employed. The generalized-gradient approximation [113], a convergence criterion for relaxation of 0.01 meV, the Blöchl correction for the total energy [100], and a cut-off of 500 eV are applied. Brillouin zone integration is carried out with a 6 × 6 × 6 Monkhorst–Pack k-point mesh [101]. 2 × 2 × 2 supercells with 64 atoms for $(V_{1-x}Al_x)_{0.5}N_{0.5}$ and 62 atoms for $(V_{1-x}Al_x)_{1-y}N_y$ with y = 0.48 or 0.52 arranged in the C#3 configuration, according to Mayrhofer *et al.* [48], are utilized. For $(V_{1-x}Al_x)_{0.52}N_{0.48}$ two nitrogen vacancies and for $(V_{0.50}Al_{0.50})_{0.48}N_{0.52}$ one vanadium and one aluminum vacancy are introduced. In order to obtain $(V_{0.25}Al_{0.75})_{0.48}N_{0.52}$ or $(V_{0.75}Al_{0.25})_{0.48}N_{0.52}$, two different vacancy scenarios with either two aluminum vacancies or one aluminum and one vanadium vacancy and two vanadium or one aluminum and one vanadium vacancy, respectively, are calculated and subsequently averaged. All vacancies are at *ad hoc* positions and with maximized distance between each other. Full structural relaxation is performed for every configuration and the Birch-Murnaghan equation of state [76] is utilized to obtain the equilibrium volume. Elastic constants are calculated according to the method of Music *et al.* [77] by determining shear elastic constants $(C_{11}-C_{12})/2$ and C_{44} applying volume conserving distortions δ = -0.02, -0.01, 0.01, 0.02 and Hill's approximation [80]. Stress-state and temperature dependent elastic moduli are determined using the Debye-Grüneisen model [81]. Here, the Helmholtz free energy (F) can be expressed as

(19) $$F = E_0 - Nk_BT\left[3\left(\frac{T}{D}\right)^3\int_0^{\frac{D}{T}}\frac{x^3}{e^x-1}dx - 3\ln\left(1-e^{-\frac{D}{T}}\right) - \frac{9D}{8T}\right],$$

where E_0, N, k_B, T, and D refer to the total energy obtain by the DFT calculations at ground state, number of atoms in the cell, the Boltzmann constant, absolute temperature, and the Debye temperature, respectively. By fitting the free energy – volume data at each temperature using the Birch–Murnaghan equation of state [76], the temperature dependent bulk moduli are obtained, which can be converted into elastic moduli using Poisson´s ratios [45, 103]. The stress dependency is obtained by considering a volume offset from an equilibrium volume at each temperature. The volume offset is converted into a stress value using the fitted equation of state. In order to evaluate the electronic structure and bond energies, density of states and crystal orbital Hamilton population (COHP) calculations are performed by employing the LOBSTER software package [114-116] and the ground-state data from VASP.

5.3. Results and discussion

Table 3 and Figure 13 show the effects of Al population on the metal sublattice ($0 \leq x \leq 0.75$), the N/M-ratio ($0.48 \leq y \leq 0.52$), as well as the stress state ($+2 \leq \sigma \leq -6$ GPa) on the elastic modulus of $(V_{1-x}Al_x)_{1-y}N_y$ at room temperature (300 K) as obtained from the Debye-Grüneisen model utilizing calculated Poisson´s ratio values shown in Figure S 5 b.

Table 3: Calculated elastic modulus (E) of $(V_{1-x}Al_x)_{1-y}N_y$ as a function of composition (x and y) and stress states at room temperature (300 K) employing the Debye-Grüneisen model.

Stress	**$E(V_{1-y}N_y)$ [GPa]**			**$E((V_{0.75}Al_{0.25})_{1-y}N_y)$ [GPa]**			**$E((V_{0.50}Al_{0.50})_{1-y}N_y)$ [GPa]**			**$E((V_{0.25}Al_{0.75})_{1-y}N_y)$ [GPa]**		
[GPa]	y=0.48	y=0.50	y=0.52	y=0.48	y=0.50	y=0.52	y=0.48	y=0.50	y=0.52	y=0.48	y=0.50	y=0.52
+2	377	376	397	431	447	446	437	451	446	448	469	447
0	391	388	411	447	464	463	455	469	464	467	488	466
-2	406	400	426	464	482	479	472	486	481	485	506	484
-4	420	413	440	480	499	496	489	504	498	503	524	502
-6	434	424	455	496	516	512	506	521	515	521	542	519

This allows for a direct comparison with experimental elastic moduli, which are commonly measured at room temperature as the temperature dependency of the elastic modulus (see Figure S 5 d) is considered. Overall, the combined effect of increasing the Al concentration and varying the stress state from tensile to compressive causes an elastic modulus increase by 44 %.

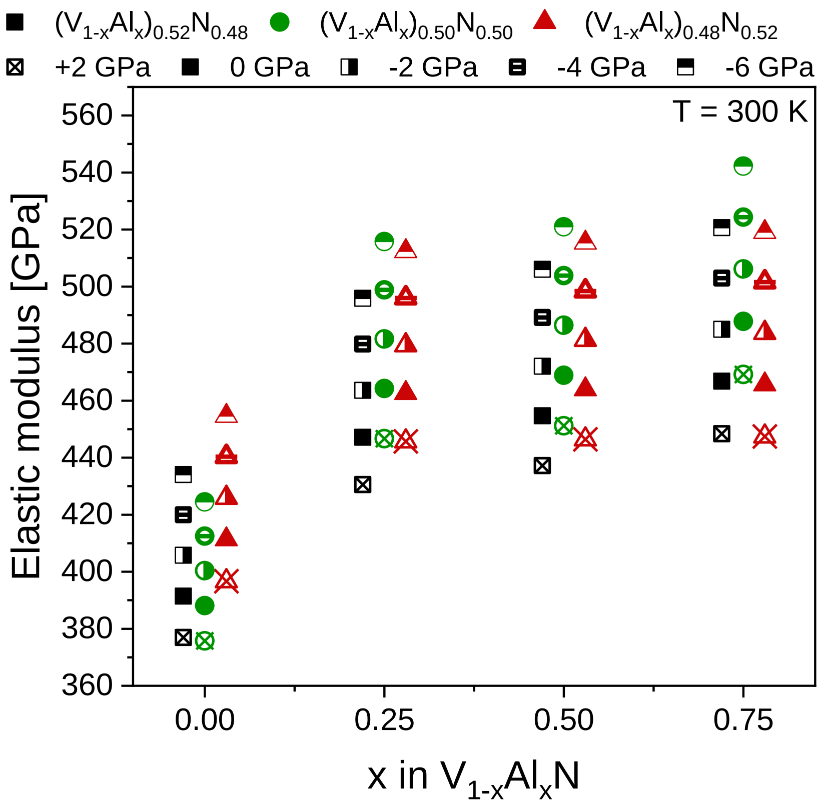

Figure 13: Elastic modulus of $(V_{1-x}Al_x)_{1-y}N_y$ as a function of x for different stoichiometries (y = 0.48, 0.50, and 0.52) and stress states at a temperature of T=300 K obtained by the Debye-Grüneisen model.

First, the effect of the Al population induced changes in elastic modulus are evaluated. If the Al content x is increased from 0 to 0.25 for stress free $(V_{1-x}Al_x)_{0.5}N_{0.5}$, a 20 % increase in elastic modulus from 388 to 464 GPa is obtained. Increasing the Al content further to x = 0.5 and x = 0.75 only results in a 1 % and 5 % increase to 469 and 488 GPa, respectively. This initial drastic increase associated with Al incorporation in VN is rationalized based on the concomitantly occurring electron structure change: The electronic structure of the binary VN configuration is dominated by V3d-N2p orbital overlap, giving rise to sp^3d^2 hybridization (Figure 14 a).

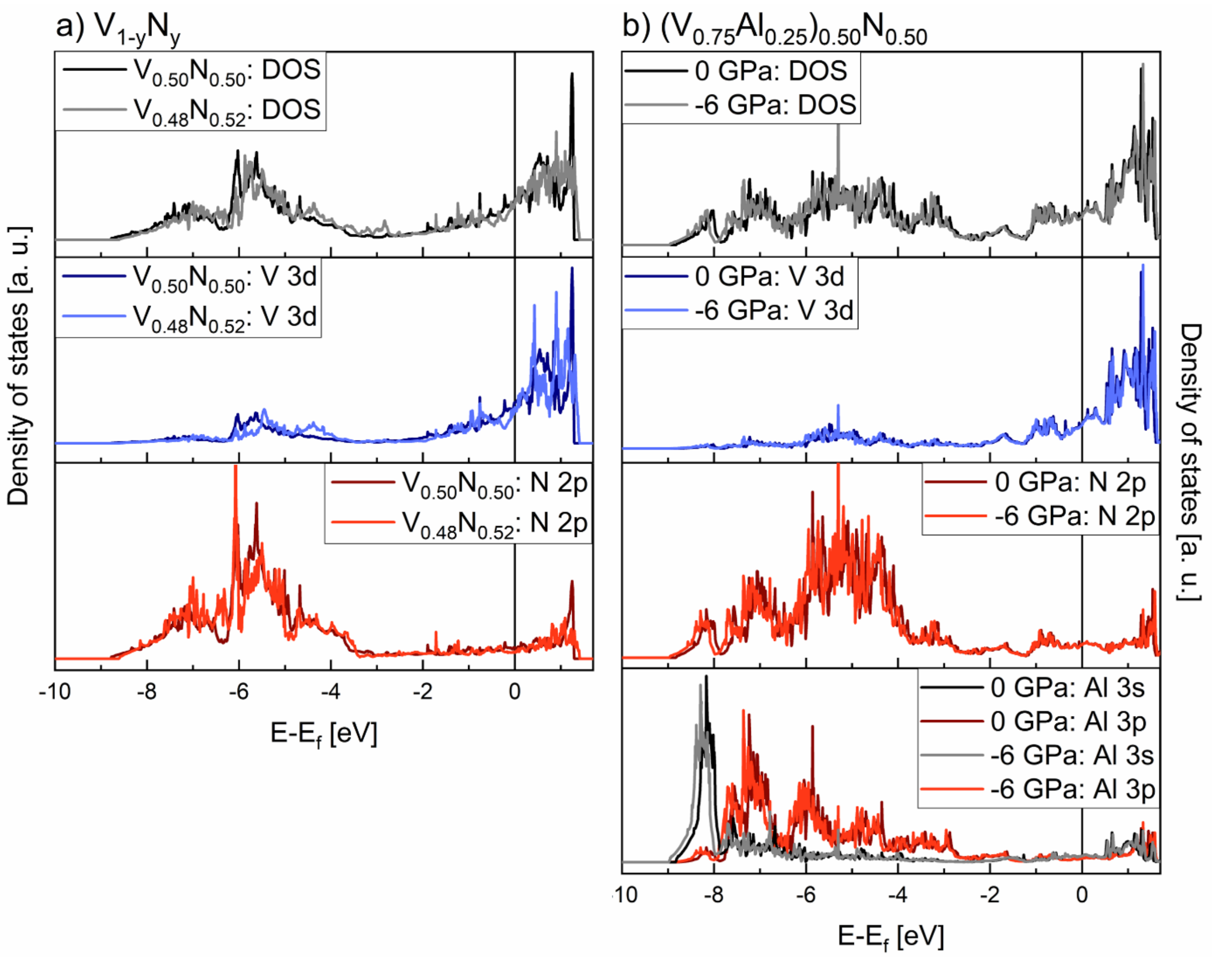

Figure 14: Total and partial density of states (DOS) analysis for $V_{0.50}N_{0.50}$, $V_{0.48}N_{0.52}$, and $(V_{0.75}Al_{0.25})_{0.50}N_{0.50}$. E_f designates the Fermi energy.

This is consitent with literature [117, 118]. While upon Al incorporation the bonding nature remains unchanged, significant bond energy variations are induced. Based on total and partial density of states (DOS), strong sp^3d^2 hybridization between Al and N in the energy range of -7 to -9 eV for $(V_{0.75}Al_{0.25})_{0.5}N_{0.5}$ (Figure 14 b) can be observed, whereas $V_{0.5}N_{0.5}$ exhibits far less occupied states in this energy range (Figure 14 a). As states in this energy region contribute towards strong covalent bonding in the compound and Al-N hybridization is lower in energy than that of V-N, the stiffness increase upon Al incorporation in VN can be rationalized.

Depending on the population of Al on the metal sublattice, variations in N/M-ratio affect the elastic modulus differently (see Figure 13). While for $V_{1-y}N_y$ an anomalous increase in elastic modulus from 388 GPa ($y = 0.5$) to 391 GPa ($y = 0.48$) and 411 GPa ($y = 0.52$) can be observed, a decrease in elastic modulus is obtained for Al contents of $x \neq 0$ by up to 14 GPa, being in agreement with previous calculations for $(V_{0.5}Al_{0.5})_{1-y}N_y$ [56] and $(Ti_{1-x}Al_x)_{1-y}N_y$ [119, 120], and is rationalized based on the fact that six bonds are broken when a vacancy is formed [119], which weakens the overall bond strength density. Stoichiometric VN as well as other isostructural nitrides such as NbN and TaN exhibit a dynamical instability [121]. For $V_{1-y}N_y$ [117, 122, 123] as well as for $Ta_{1-y}N_y$ and $Mo_{1-y}N_y$ [124], a stabilization of the NaCl-structured configuration was suggested due to the presence of vacancies, however, the influence of vacancies on mechanical properties for $V_{1-y}N_y$ were not considered. To identify the cause for the anomalous stiffness increase upon vacancy formation, partial and total DOS are calculated for $V_{0.5}N_{0.5}$ and $V_{0.48}N_{0.52}$ (Figure 14 a). However, no significant changes in the DOS between $V_{0.5}N_{0.5}$ and $V_{0.48}N_{0.52}$ can be observed in Figure 14 a, which is why the average bond distance and energy for one vanadium atom and its six surrounding nitrogen neighbors in the vicinity of a nitrogen vacancy are considered. The average bond distance and energy are obtained from COHP calculations, where the integrated COHP (ICOHP) up to the Fermi level (E_f) serves as an indicator for the bond energy. A decrease in the bond distance of 0.5 % from 2.06 to 2.05 Å and an decrease in the ICOHP of 6 % from -2.69 to -2.85 eV for $V_{0.50}N_{0.50}$ and $V_{0.48}N_{0.52}$, respectively, are obtained, implying bond strengthening. Hence, bond strengthening is the origin of the anomalous stiffness increase upon vacancy formation in $V_{1-y}N_y$.

Finally, variations in the stress state from +2 GPa (tensile stress) to -6 GPa (compressive stress) are considered (see Figure 13). Stress free $(V_{0.75}Al_{0.25})_{0.5}N_{0.5}$ possesses an elastic modulus of 469 GPa, which decreases by 4 % to 451 GPa for +2 GPa and increases to 487, 504, and 521 GPa for -2, -4, and -6 GPa, respectively, and hence by up to 11 %. This is in good agreement with experimental results for $V_{0.5}Al_{0.5}N$ [57] which indicate a stress induced increase in elastic modulus of 35 GPa for a compressive stress offset of -4.6 GPa. The origin of the stress dependency of the elastic modulus can be understood based on the electronic structure. Figure 14 b depicts total and partial DOS for $(V_{0.75}Al_{0.25})_{0.5}N_{0.5}$ at a stress free and -6 GPa compressive stress state. For the -6 GPa compressive stress state, the total and partial DOS of $(V_{0.75}Al_{0.25})_{0.5}N_{0.5}$ are shifted towards lower energy implying stress induced bond strengthening and hence an increasing stiffness. Overall, elastic moduli between 375 and 541 GPa and thus with a spread of 31 % are obtained for $(V_{1-x}Al_x)_{1-y}N_y$, if the influence of the Al concentration ($0 \leq x \leq 0.75$), N/M-ratio ($0.48 \leq y \leq 0.52$), and stress state ($+2 \leq \sigma \leq -6$ GPa) are considered. Compared to the extensive overall spread of 58 % observed for reported elastic moduli in the literature, which comprises a spread in elastic modulus of 294 – 415 GPa at x = 0.4 and 428 – 599 GPa at x = 0.5, the predicted range of elastic modulus at x = 0.5 of 437 – 521 GPa only in parts accounts for this reported spread. The origin of the 15 % larger reported elastic modulus originates most likely from errors associated with the nanoindentation measurements or from modifications of the thin film composition by post deposition chemical reactions with the atmosphere [125] provided that the reaction products formed exhibit a larger elastic modulus than $(V_{1-x}Al_x)_{1-y}N_y$. The 33 % lower reported elastic modulus may be attributed to other elastic modulus influencing parameters such as density and porosity [108, 126], grain size [108], preferred orientation [127], or impurity incorporation from residual gas during thin film growth [56, 128], composition modifications due to atmosphere exposure after thin film growth [125], which were not considered by DFT in this work. Exemplarily, results from Shaha *et al.*, which reveal a 9 % decrease in elastic modulus due to 7 at.% oxygen incorporation in $V_{0.5}Al_{0.5}N$ [56] and results from Knudsen, which show a decrease in elastic modulus of 13 % caused by the presence of 4 % porosity in alumina [126], reveal the impact of these parameters on the elastic modulus. Hence, reports on the elastic modulus of VAlN without information of the stress state as well as accurate and precise composition measurements both with respect to the metal ratio as well as to the non-metal to metal ratio will remain difficult to be interpreted. It is reasonable to assume that these findings are of relevance for other transition metal Al nitiride and oxynitride thin films.

6. Conclusions

In chapter 3 and 4, the effect of target power density, substrate bias potential, and substrate temperature on the chemical composition, phase formation, microstructure evolution, and mechanical properties of sputtered Cr-Al-C thin films from Cr-Al-C composite targets was investigated. This enabled the implementation of a methodology to design a processing parameter specific composite target composition for the industrial-scale deposition of multi-element thin films and allowed to holistically address requirements for the utilization of Cr_2AlC MAX-phase coatings for energy conversion applications such as the large-area deposition of dense and single phase coatings. In short, it was identified that increasing the target peak power density by two orders of magnitude

I) enhances compositional deviations between target and thin film by up to factor 3 and

II) results in coatings with superior density and hence larger elastic moduli.

I) By systematically varying the target power density, substrate bias potential and substrate temperature, the effect on the composition of DC- and HPPMS deposited thin films from a Cr-Al-C composite target was studied. Independent of the applied target power density, all thin films deposited at floating potential exhibited similar compositions, which are Cr enriched and Al and C deficient compared to the target composition. As the substrate bias potential and temperature is increased, enhanced Al deficiencies of up to a factor of 4.1 for HPPMS (373 W/cm²) compared to a factor of 1.6 for DCMS (2.3 W/cm²) are observed. At room temperature, the Al deficiency is attributed to preferential re-sputtering of Al triggered by ion bombardment, which is enhanced for higher target power densities due to the 3.4 times higher time-averaged energy flux and an approximatively 50 times higher peak ion flux. At elevated temperatures, thermal desorption of Al is suggested to be active in addition to preferential re-sputtering of Al, which is more pronounced at higher target power densities due to periodic atomic scale heating. Hence, it is evident that the composition of these films sputtered from the here employed composite target is strongly affected by the deposition conditions and that for a certain intended film composition - for example Cr_2AlC - a processing parameter specific composite target composition is required.

II) The effect of target power density and substrate bias potential on the phase formation, microstructure evolution and mechanical properties of Cr_2AlC thin films utilizing a split $Cr_{0.46}$-$Al_{0.25}$-$C_{0.29}$/$Cr_{0.15}$-$Al_{0.75}$-$C_{0.10}$ target was systematically studied. Cr_2AlC MAX-phase thin films were obtained at a floating potential by DCMS and HPPMS. While the DCMS coating possesses a Young´s modulus of 292 ± 39 GPa due to the partially under-dense and coarse-grained columnar microstructure, the HPPMS coating exhibits a dense and fine-grained columnar microstructure with a Young´s modulus of 363 ± 26 GPa, which is in excellent agreement with the *ab initio* data for -2 GPa compressive stress of 367 GPa. The dense microstructure for HPPMS indicates an increased surface diffusivity due to the higher energy input during HPPMS, which may also cause compressive residual stress. As the substrate bias is decreased for the DCMS depositions, a densification of the microstructure, the formation of the disordered solid solution $(Cr,Al)_2C_x$ below -100 V substrate bias, and an increase in Young´s modulus (327 ± 23 GPa at -60 V) and a subsequent decrease (260 ± 36 GPa at -400 V) is caused by the complex interplay of Ar-ion bombardment induced effects.

For HPPMS, a continuous increasing phase fraction of $(Cr,Al)_2C_x$ together with decreasing Young´s moduli to 327 ± 20 GPa at -200 V is observed and may again be attributed to the intricate combination of ion bombardment induced effects. Thus, it is evident that there is an optimum moderate ion energy for the formation of dense Cr_2AlC MAX-phase coatings. Too low ion energy results in the formation of under-dense coatings, while too high ion energy gives rise to the formation of the disordered $(Cr,Al)_2C_x$ solid solution in addition to the MAX-phase Cr_2AlC. Furthermore, this combinatorial study paves the way for designing a processing parameter specific composite target composition which allows to holistically address application related requirements such as the deposition of dense, single phase coating at substrate temperatures compatible with metallic substrates.

In chapter 5, the extensive and theoretically unexplained spread in experimentally obtained elastic moduli ranging from 254 to 599 GPa as reported in literature for $(V_{1-x}Al_x)_{1-y}N_y$ was studied by density functional theory employing the Debye-Grüneisen model. By considering the effect of the Al concentration ($0 \leq x \leq 0.75$), N/M-ratio ($0.48 \leq y \leq 0.52$), and stress state, the elastic modulus of metastable $(V_{1-x}Al_x)_{1-y}N_y$ at room temperature was calculated. Thereby, it was predicted that increasing the Al content from $x = 0$ to $x = 0.75$ results in an increase in elastic moduli from 388 to 488 GPa. This 26 % increase is caused by strong sp^3d^2 hybridization between Al and N. Variations of the N/M-ratio of VN result in an anomalous stiffness increase from 388 GPa ($y = 0.50$) to 411 GPa ($y = 0.52$). This up to 6 % increase can be rationalized considering the vacancy induced bond distance decrease. Vacancy formation in $(V_{0.5}Al_{0.5})_{1-y}N_y$ on the other hand results in an up to 3 % decrease in elastic modulus, e.g. for $(V_{0.5}Al_{0.5})_{1-y}N_y$ from 469 GPa ($y = 0.5$) to 455 GPa ($y = 0.48$). Stress variations from +2 GPa to -6 GPa cause an increase in elastic modulus e.g. for $(V_{0.5}Al_{0.5})_{0.5}N_{0.5}$ by up to 70 GPa and hence by 13 % due to shifts in the density of states towards lower energies implying bond strengthening. Overall, elastic moduli between 375 and 541 GPa and thus a spread of 31 % are obtained for $(V_{1-x}Al_x)_{1-y}N_y$ ($0 \leq x \leq 0.75$, $0.48 \leq y \leq 0.52$, and $-6 \leq \sigma \leq 2$ GPa), which in part explains the extensive spread of 58 % in reported elastic moduli ranging from 254 to 599 GPa. The remaining discrepencies may originate from other elastic modulus influencing phenomena including the presence of extended defects for instance grain boundaries and nano pores, modifications of the composition by impurity incorporation during growth and post deposition atmosphere exposure, and the growth of underdense morphologies. Hence, experimental reports on the elastic modulus of VAlN without accurate and precise information on the stress state and composition will be difficult to interpret. Furthermore, these findings may be relevant for other transition metal Al nitrides and oxynitride thin films.

7. Future work

Several exciting questions were raised during this work:

1. **Where does the apparent C-deficiency and Cr-enrichment during magnetron sputtering of Cr_2AlC thin films from composite targets originate from?**

Based on the compositional results obtained for Cr-Al-C thin films by ERDA measurements, which were presented in chapter 3, all coatings exhibit a Cr-enrichment and a C-deficiency. The origin is still unclear. It may be speculated that the Cr-enrichment and C-deficiency is caused by a non-steady state mode of the target or in part may be a result of misinterpretation due to possible inaccurate chemical compositional analysis, while other effects such as carbon reacting with residual oxygen and thus forming CO or CO_2, angular distribution or gas phase scattering effects during sputtering may be excluded based on preliminary results. A possible explanation may be an inaccurate chemical compositional analysis, as preliminary compositional results indicate a low accuracy when measuring the same Cr-Al-C thin film sample utilizing different techniques. ERDA measurements revealed a composition of 55.7 at.% Cr, 26.2 at.% Al, and 18.1 at.% C, while wavelength-dispersive X-ray spectroscopy (WDS) yielded a composition of 53.2 at.% Cr, 23.5 at.% Al, and 23.3 at.% C and Rutherford backscattering (RBS) a composition of 45 at.% Cr, 25 at.% Al, and 30 at.% C. Thus, a spread of 12 at.% in C is obtained, which highlights the necessity for accurate and precise chemical compositional analysis. Thus, in a first attempt to identify the origin of the apparent Cr-enrichment and C-deficiency, a systematic compositional analysis study based on a multi-method approach utilizing ion beam analysis techniques such as RBS, ERDA, EBS, and particle-induced X-ray emission (PIXE) as proposed by Moro *et al.* [129] should be conducted. To further validate these results, secondary-ion mass spectrometry (SIMS), nuclear resonance analysis (NRA) or atom probe tomography APT) could be used. Based on these results, a further study may be conducted to investigate the effect of a non-steady state mode of the target by sputtering a Cr-Al-C target and tracking the temporal compositional evolution of the obtained thin films.

2. How does substrate rotation affect compositional deviations between composite targets and thin films?

It has been shown in chapter 3, that target power density, substrate bias potential, and substrate temperature variations drastically affect compositional deviations between target and thin films. Furthermore, Mráz *et al.* have shown a strong pressure-to-distance product as well as angular distribution effect on the composition of sputtered thin films from a Cr_2AlC compound target [4], which is also known for other systems such as Mo_2BC [28] and TiB_2 [3]. Another decisive deposition parameter for industrial depositions - substrate rotation - has yet not been considered. However, as the samples constantly move through areas with high and low plasma densities as well as high and low particle fluxes and additionally constantly vary the target-to-substrate distance as well as the angle relative to the targets, compositional deviations between thin films and targets and/or compositional modulations within the samples may be expected, as reported by Hans *et al.* for TiAlON [130]. To systematically study this effect, depositions utilizing 2-fold and 3-fold substrate rotation as well as different target power densities and substrate bias potentials should be conducted and subsequently analyzed regarding their spatially-resolved (APT and high-resolution TEM) as well as local (ion beam analysis techniques) chemical composition.

3. **How do mass differences in multi-element composite targets affect compositional deviations between target and thin films?**

As concluded in chapter 3, the target power density, substrate bias potential, and substrate temperature drastically affect compositional deviations between the $Cr_{0.50}$-$Al_{0.27}$-$C_{0.23}$ composite target and thin films due to preferential re-sputtering and thermally induced desorption of Al. In general, the energy transfer during (re-)sputtering with Ar or film-forming species, the gas phase transport as well as the angular distribution function is mass dependent. Thus, the question arises how different mass ratios between the composite target atoms or different sputtering gas masses (e.g. krypton or xenon) may affect the observed compositional deviation between composite target and thin film. In order to critically appraise this question, a systematically study utilizing different composite targets (e.g. $Zr_{0.50}$-$Al_{0.25}$-$C_{0.25}$ or $Hf_{0.50}$-$Al_{0.25}$-$C_{0.25}$) and sputtering gases should be conducted and may help to generate a fundamental understanding of compositional deviations between composite targets and thin films.

4. **What is the maximum Al solubility in HPPMS deposited Cr_2AlC thin films?**

The combinatorial depositions carried out for the synthesis of nearly stoichiometric Cr_2AlC thin films utilizing HPPMS in chapter 4 may imply larger Al solubilities of up to 39 at.% in Cr_2AlC than reported by Mertens *et al.* of 31 at.% for DCMS deposited samples [104]. However, a critical appraisal of the Cr_2AlC phase formation instead of the disordered solid solution $(Cr,Al)_2C_x$ by SAED is pending. On the basis of Cr_2AlC phase formation, large Al solubilities may improve the oxidation resistance of Cr_2AlC thin films by postponing the chromium carbides formation below the protective alumina scale. Thus, identifying the maximum Al solubility range in Cr_2AlC by utilizing a combinatorial deposition setup, varying the HPPMS deposition parameters and subsequently analyzing the samples by HR-TEM and APT to identify the location of the excess Al may be of interest for future industrial applications of Cr_2AlC thin films.

5. What is controlling the texture evolution of Cr_2AlC thin films during growth?

It has been shown in chapter 4, that industrial-scale DCMS and HPPMS deposited Cr_2AlC thin films on WC substrates mainly possess a (110) texture. The same texture can also be observed on single-crystalline MgO (100) substrates (Figure 15 a) under comparable deposition conditions. However, if the deposition conditions are changed and the pressure-to-distance product is increased from approximately 1 - 3 Pa*cm to 18 Pa*cm and the deposition rate is decreased from approximately 80 nm/min to 15 nm/min, a change towards a (103) texture can be observed. Furthermore, depositions carried out in a lab-scale deposition chamber (Figure 15 c and d) utilizing DCMS, a pressure-to-distance product of 18 Pa*cm, and a deposition rate of 8 nm/min yield different textures depending on the deposition time and hence film thickness. While the 1200 nm thick sample (Figure 15 c) possesses a (110) texture, the 500 nm thin sample exhibits a (002) texture. Different texture evolution for different deposition parameters have also been reported in literature [24, 41, 104, 131, 132] and Naveed *et al.* have correlated this variation in preferred orientations to accumulation of surface and strain energy during the coating process [131], even though no experimental evidence was provided. Stress measurements performed on the lab-scale deposited samples in Figure 15 c and d revealed compressive stress states of -5.2 and -3.2 GPa for 500 and 1200 nm thick films, respectively, which may be an indication for the proposed strain energy dependent texture evolution.

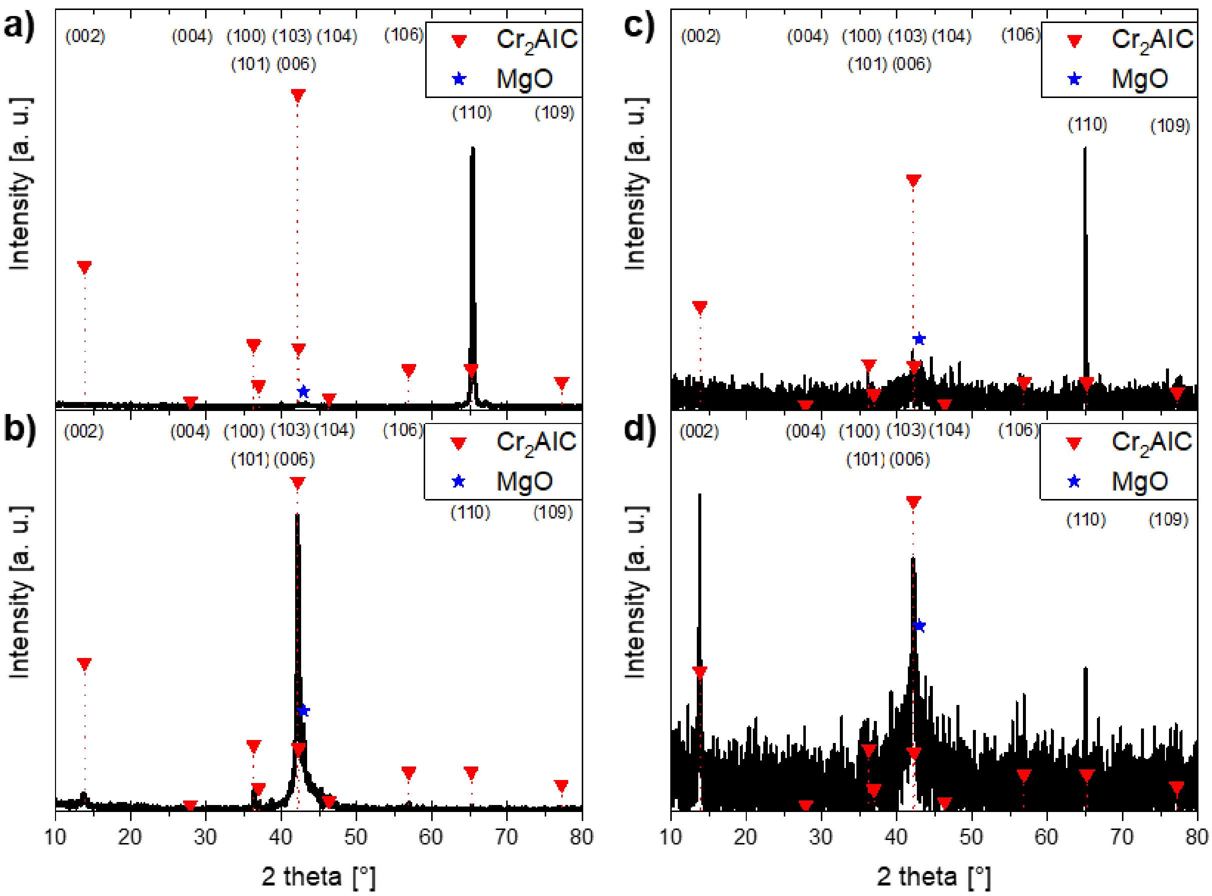

Figure 15: Diffractograms of Cr_2AlC thin films (Cu K_α) deposited in an industrial-scale (a and b) and a lab-scale (c and d) deposition system. The corresponding deposition parameters and chemical compositions (Table S1) can be found in the appendix (chapter 8).

Thus, a systematic study considering variations in deposition parameters as well as film thicknesses should be conducted. To track the strain evolution during film growth, *in situ* multi-beam optical stress sensor (MOSS) measurements or *ex situ* synchrotron nanodiffraction experiments [133] should be performed. Furthermore, DFT calculations could reveal the surface energies of the (002), (100), (103), and (110) planes in a stress-free as well as stress exposed state. Thus, based on the correlative experimental and theoretical approach, the proposed surface and strain energy notion for the texture evolution of Cr_2AlC thin films may be validated.

6. Can the synthesis temperature for the deposition of crystalline Cr_2AlC thin films be further decreased by utilizing HPPMS while keeping the densities comparable to high temperature depositions?

It has been shown in chapter 4 that Cr_2AlC thin films can be synthesized at 560 °C substrate temperature utilizing DCMS and HPPMS, which is close to the lowest Cr_2AlC thin film formation temperatures of 520 °C reported by Su *et al.* [132] and 550 °C by Walter *et al.* [2]. Lower Cr_2AlC synthesis temperature may be found in literature, however, these reports lack a proof for the phase formation of Cr_2AlC instead of the disordered solid solution $(Cr,Al)_2C_x$, which already forms at 300 °C according to Shtansky *et al.* [134]. It is well known and was shown for the deposition of Cr-Al-C thin films in chapter 3, that HPPMS can provide larger energy inputs during film growth compared to DCMS and thus may enable a low temperature synthesis of Cr_2AlC, as it was shown for Mo_2BC by Bolvardi *et al.* [135]. Therefore, a systematic study of HPPMS parameters in combination with different substrate bias potentials and deposition temperatures on the phase formation of Cr_2AlC, which may be verified by HR-TEM or synchrotron nanodiffraction, should be conducted. This may help to lower the synthesis temperature of Cr_2AlC while keeping the thin film density comparable, which is crucial for the mechanical properties, as discussed in chapter 4.

7. Why do deposition parameter variations influence the composition of Cr_2AlC thin films differently than TMAlN (TM = V and Cr)?

Based on the results presented in chapter 3, where a significant effect of deposition parameter variations, such as substrate bias potential, on the composition of Cr-Al-C thin films has been observed, the notion of deposition parameter influences on the chemical composition of sputtered thin films has been adapted in a preliminary study to transition metal aluminum nitrides such as VAlN, CrAlN, and CrAlSiN. In contrast to the Cr_2AlC system, only minor compositional effects upon deposition parameter variations of a few atomic percent have been observed, as it can be seen in the APT concentration profile in Figure 16, where the substrate bias potential has been varied from floating to -140 V.

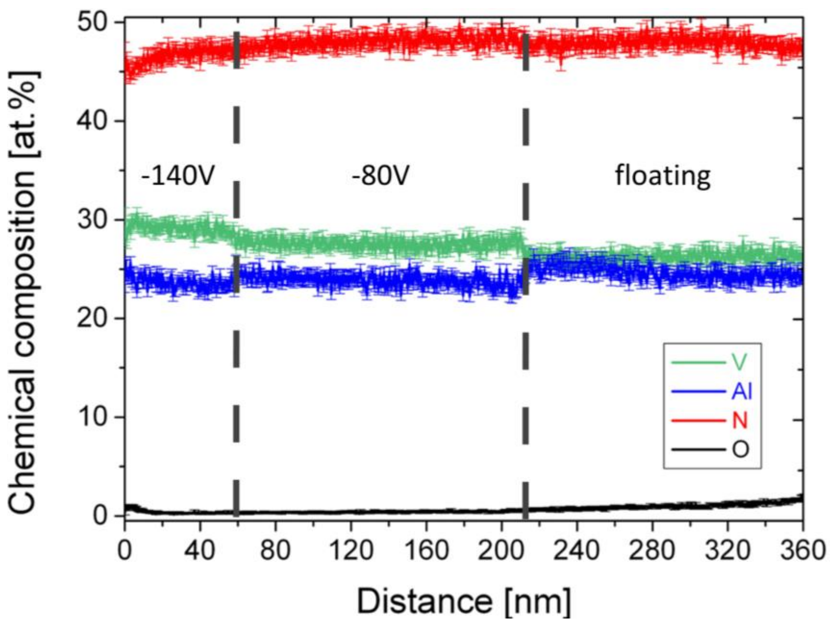

Figure 16: Atom probe tomography concentration profile for a distance of 360 nm in the growth direction of VAlN. Three different substrate bias potentials (floating, -80, and -140 V) have been used during the deposition. The corresponding deposition and analysis parameters can be found in the appendix (chapter 8).

But how can this difference be rationalized? It may be speculated, that different bonding characteristics of Al are causing this difference. While Al is metallically bonded to Cr in Cr_2AlC, it possesses covalent and ionic bonds to N in TMAlN, which are stronger compared to metallic bonds in Cr_2AlC. Thus, to validate this hypothesis, molecular dynamics DFT simulations studying the effect of ion-surface interactions upon ion bombardment for Cr_2AlC and TMAlN surfaces as proposed by Music *et al.* for CrAlN [136] may be performed.

8. Appendix

In the following, in detail structural analysis of the growth characteristics as well as grain size distribution analysis, which were performed on thin film cross-sections of the three HPPMS samples grown at floating, -100, and -200 V substrate bias as discussed in **chapter 4**, are shown. These investigations were carried out with a FEI Tecnai F20 transmission electron microscope (TEM) operated at 200 kV. Selected area electron diffraction (SAED) patterns were recorded with a Veleta S04F camera from EMSIS GmbH (Münster, Germany). Analysis of crystallite orientation, phase mapping, and grain size distributions were performed by scanning electron nanobeam diffraction (SEND) using a retrofitted ASTAR-system from NanoMEGAS SPRL (Brussels, Belgium). The areas for SEND analysis were about 1x1 μm^2 in size. The lateral step-to-step size was 4.5 nm.

Figure S1 depicts a colorized composite of the three superimposed SAED patterns obtained from the HPPMS grown samples at floating, -100 and -200 V.

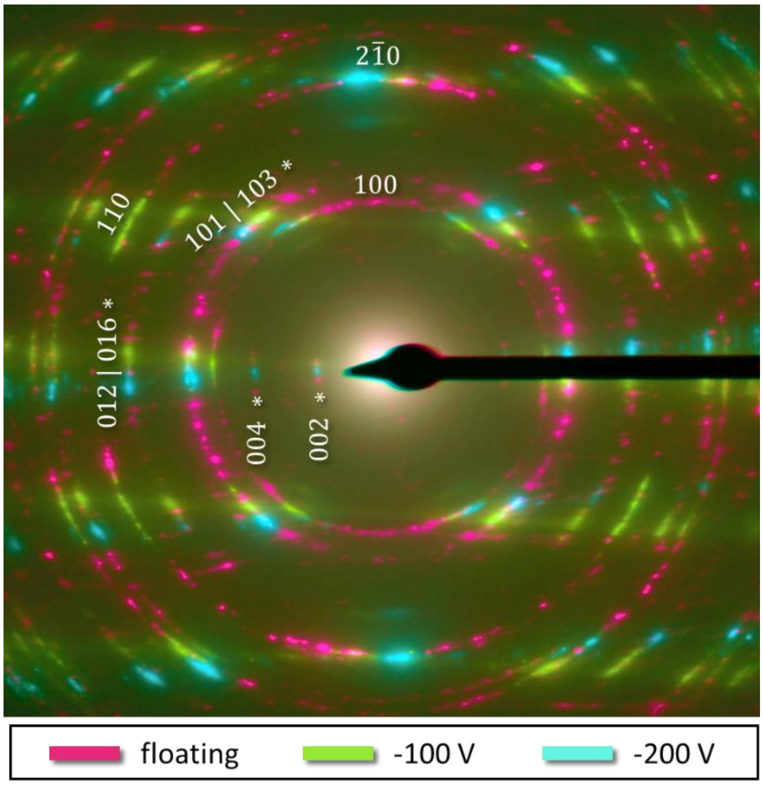

Figure S1: Colorized composite of the three superimposed SAED patterns taken from vertical FIB cross-sections of the HPPMS grown samples at floating, -100, and -200 V. The given Laue indices refer to both Cr_2AlC and the disordered solid phase. Starred indices (∗) are unique reflexes for Cr_2AlC stemming from the 3 times elongated c-axis of the Cr_2AlC unit cell.

The SAED patterns obtained for the specimens grown at -100 and -200 V substrate bias indicate pronounced preferred orientation (texture) with a growth direction along the hexagonal *a*-axis, i.e. stacking of $(2\bar{1}0)$ planes as shown in the structure model in Figure S2 a. The Laue reflections marked by stars in Figure S1 with indices 002 and 004 prove the presence of Cr_2AlC in all three specimens, but cannot be used to estimate the amount of Cr_2AlC, as the appearance and intensity of the 002 and 004 indicator reflections in cross-section samples is coincidental, since the *c*-axis is allowed to rotate arbitrarily parallel to the $(2\bar{1}0)$ planes / around the a-axis.

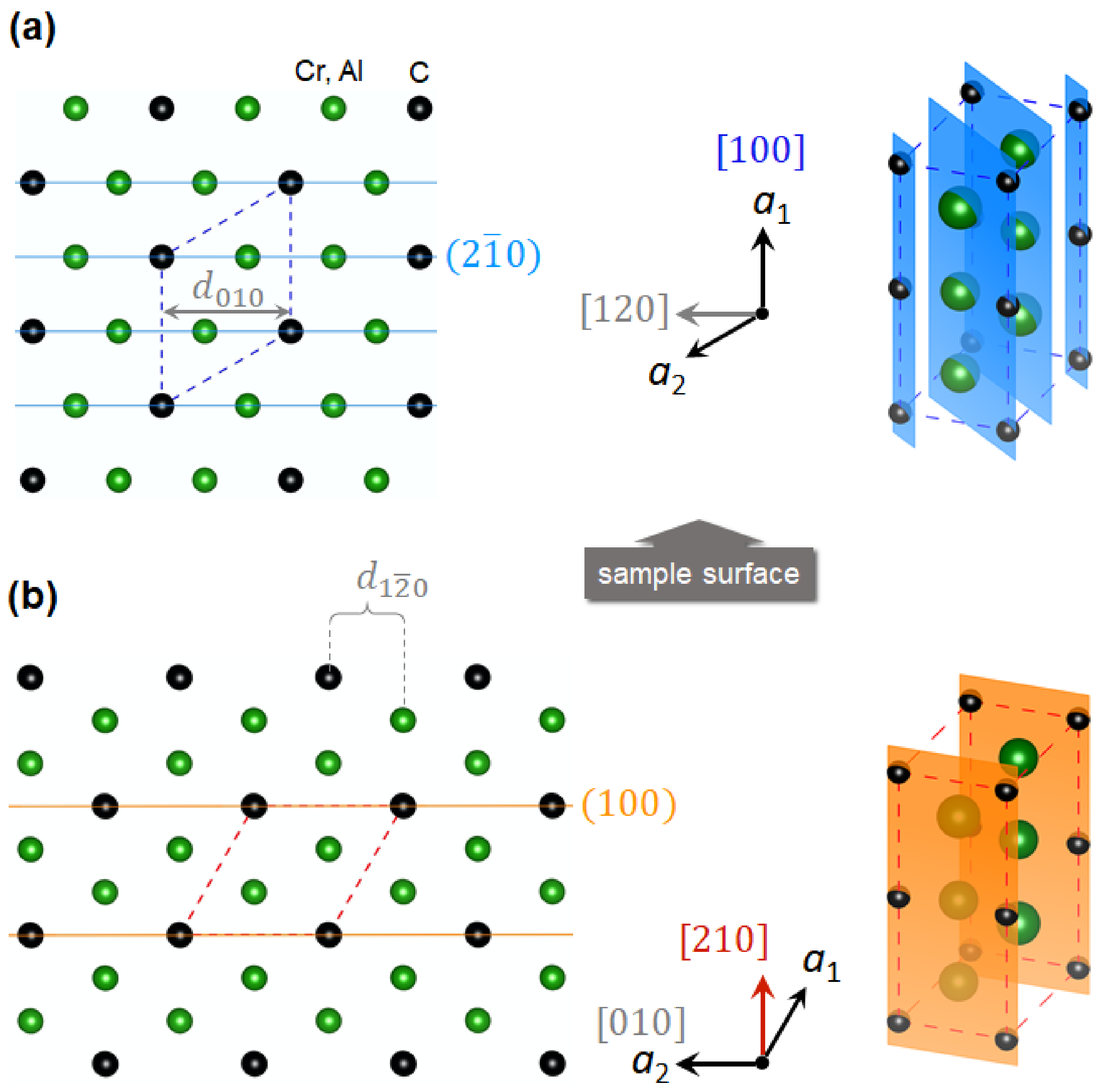

Figure S2: (a) Structural model in projection along the [001] direction (left), equivalent for both $CrAl_2C$ and $(Cr,Al)_2C_x$, as determined from the SAED patterns shown in Figure 9 and associated Cr_2AlC unit cell model (right). (b) Structural model as in (a) but after in-plane rotation by 30º around zone axis [001] (c axis).

This also implies that the thin film growth at floating, -100, and -200 V substrate bias proceeds by deposition of in-plane shifted $(2\bar{1}0)$ layers along the [100] stacking direction as shown in Figure S2 a. Thus, the in-plane shift direction is $[120]$, whereas the length of the in-plane shift vector is equal to the interplanar distance d_{010}. The corresponding layer-to-layer distance is determined by the $d_{2\bar{1}0}$ interplanar spacing. At floating potential, a second superimposed growth direction can be observed

(Figure S2 b), where an in-plane rotation by 30º around the [001] zone axis occurs. This is characterized by layer deposition along the [210] direction with a stacking sequence of one layer exhibiting only C atoms, followed by two layers consisting out of Cr and Al atoms. Layers that contain either C or metal atoms are shifted in-plane along [010] by the distance $d_{1\bar{2}0}$. The layer-to-layer distance in growth direction is $\frac{1}{3} \cdot d_{100}$. Hence the layer-to-layer distance along [210] is by a factor $\sqrt{3}/3$ smaller than in the other, simultaneously occurring growth direction along [100].

Both simultaneously occurring growth directions for the HPPMS deposited sample at floating potential are depicted in the sketch in the third row in Figure S3.

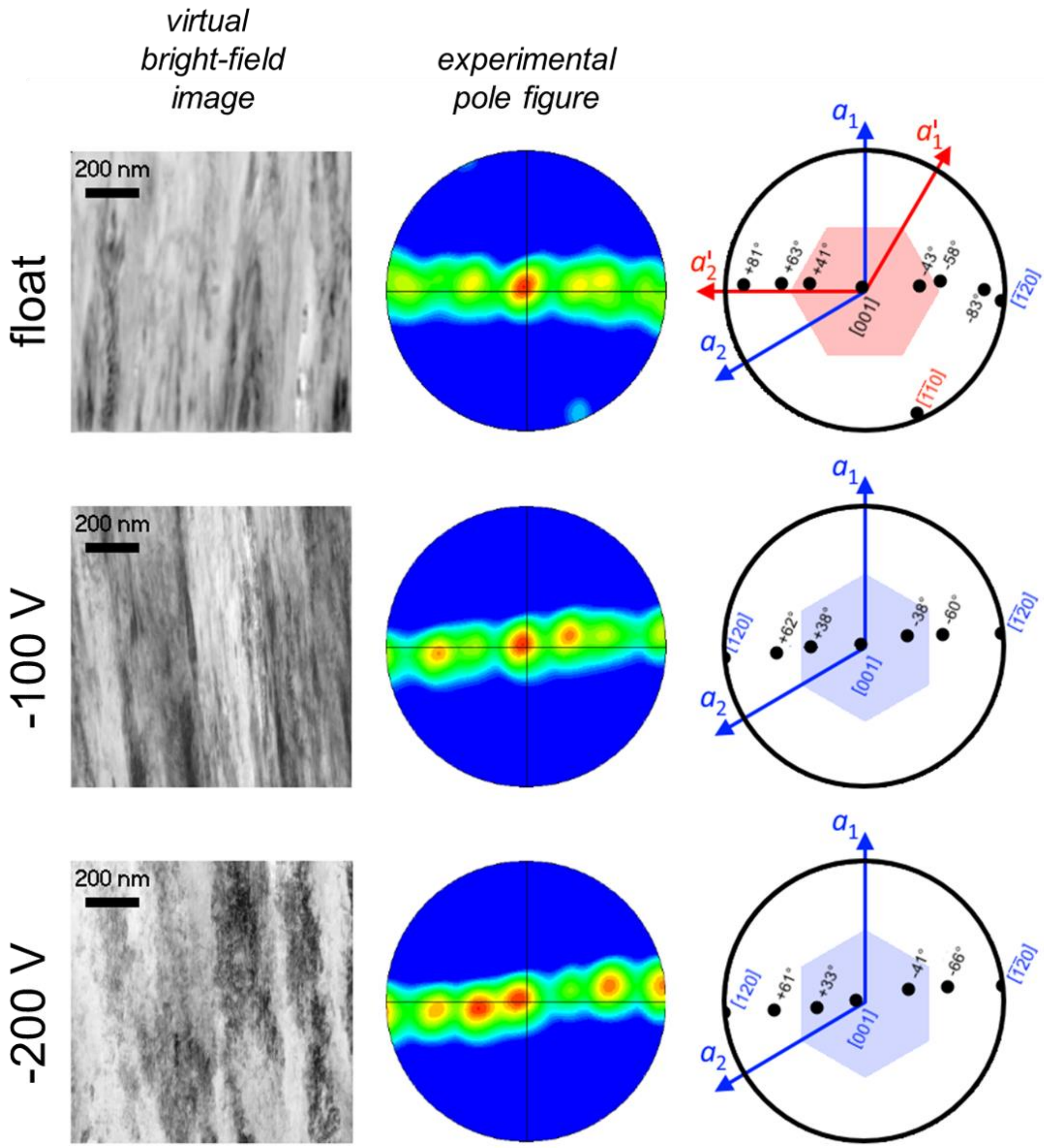

Figure S3: Results of ACOM-TEM (ASTAR, Nanomegas) analysis and interpretation for the three investigated samples. The left row of images shows the investigated sample regions as reconstructed (virtual) bright-field images from nano-beam scanning electron diffraction. The second row of images are pole figure plots obtained via the automated template matching for Cr_2AlC and disordered solid solution with the prominent [001] pole close to the centre. The row of sketches on the right side shows the measured angles between the poles in respect to the [001] pole together with the corresponding real space crystal axes as overlay.

The corresponding pole figure shows the prominent [001] direction as strong pole density maximum in the horizontal band and an additional pole density maximum located at an azimuthal position close to 30° from the south pole, which can be identified as [-1-10] if the second predominant orientation is considered. This is in agreement with the XRD results (Figure 8), as a preferred (100) and (110) orientation is observable. The suggested structural change from Cr_2AlC to $(Cr,Al)_2C_x$ with decreasing substrate bias is associated with a 3 times smaller *c*-axis and therefore a significantly reduced number of possible orientations. Accordingly, the change in the appearance of pole figures with a rather smeared horizontal band with only poorly developed pole density maxima at floating potential and well developed pole density maxima in the horizontal band at -100 and -200 V (Figure S3) may be rationalized. These well-developed pole density maxima in the pole figures for the HPPMS deposited samples at -100 and -200 V indicate pronounced preferred orientation. The pole figures are crossed by a nearly horizontal band of distinct directions which are all normal to the direction [100], which is the principal a-axis and direction of growth as discussed above.

Grain size distributions obtained from ACOM-TEM analysis for HPPMS grown samples at floating, -100, and -200 V are depicted in Figure S4. Increasing occurrence of smaller grain sizes with decreasing substrate bias can be observed.

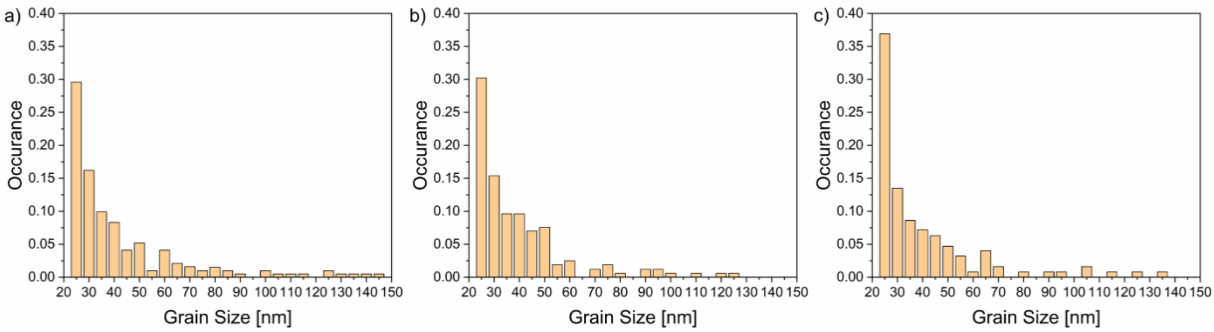

Figure S4: Grain size distribution obtained by ACOM-TEM analysis for HPPMS deposited samples at floating (a), -100 V (b), and -200 V (c).

Hereafter, the ground state bulk moduli, Poisson´s ratios and elastic moduli of $(V_{1-x}Al_x)_{1-y}N_y$ with $0 \leq x \leq 0.75$ and $0.48 \leq y \leq 0.52$ as well as for the temperature dependent elastic modulus of $(V_{0.5}Al_{0.5})_{0.5}N_{0.5}$ from DFT calculations in **chapter 5** are presented.

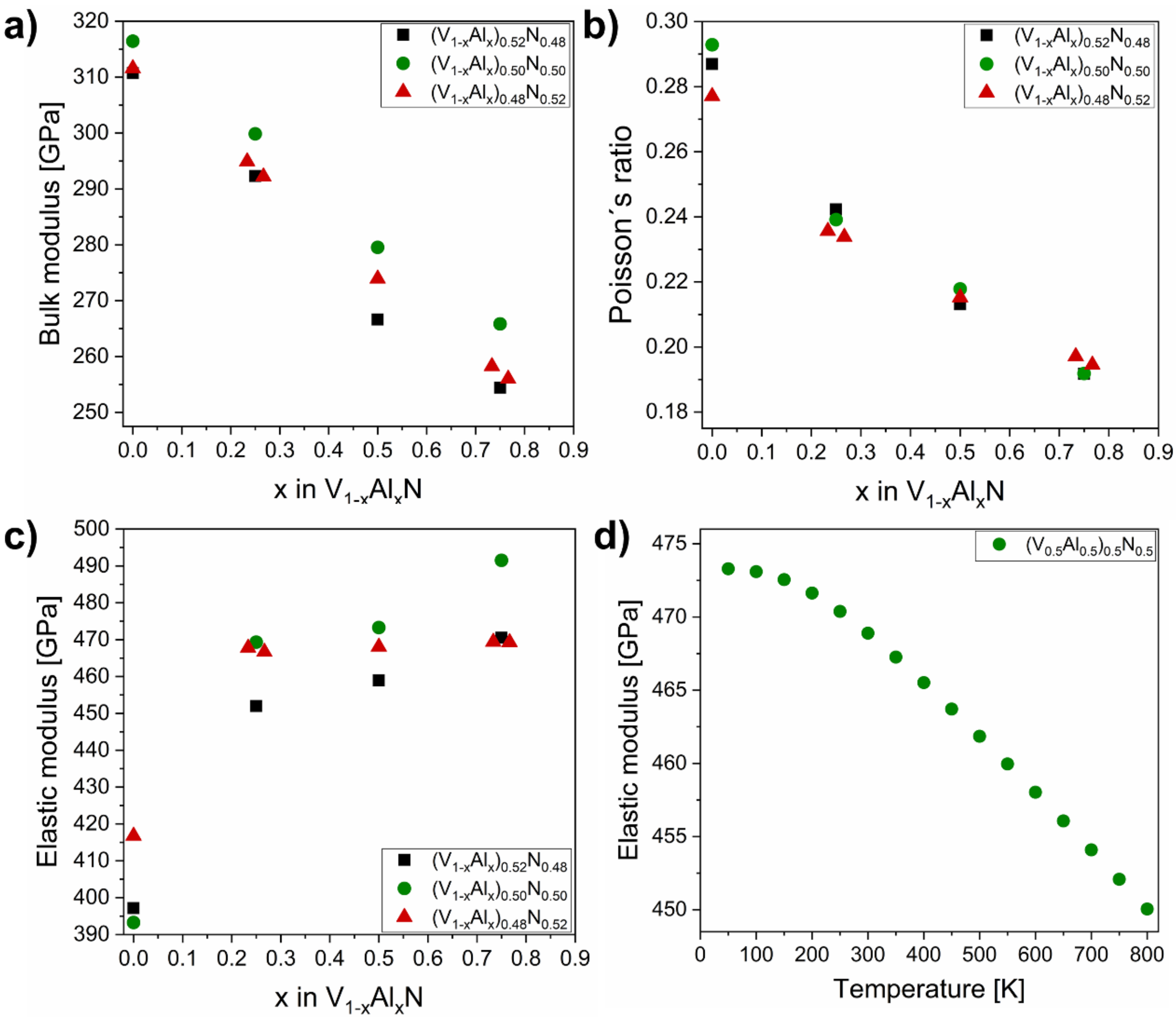

Figure S 5: Bulk modulus (a), Poisson´s ratio (b), and elastic modulus (c) at ground state for $(V_{1-x}Al_x)_{1-y}N_y$ as a function of x, as well as the temperature dependency of the elastic modulus for stress free $(V_{0.5}Al_{0.5})_{0.5}N_{0.5}$ (d).

Figure S 5 depicts the bulk modulus (a), Poisson´s ratio (b), and elastic modulus (c) at ground state for $(V_{1-x}Al_x)_{1-y}N_y$ as a function of the Al concentration x and the non-metal to metal ratio (N/M-ratio) y. The elastic modulus of $(V_{1-x}Al_x)_{0.5}N_{0.5}$ obtained at 0 K

(Figure S 5 c) increases with increasing Al concentration x and the elastic modulus of $V_{1-y}N_y$ increases upon vacancy formation, while the elastic modulus of $(V_{1-x}Al_x)_{1-y}N_y$ decreases upon vacancy formation. Hence, the same trends, as already discussed for the elastic modulus at 300 K, are obtained. The bulk modulus and the Poisson ratio decrease with increasing Al concentration x by 16 % and 35 %, respectively. As the elastic modulus (E) is linked to the bulk modulus (B) and Poisson´s ratio (ν) via E=3*B*(1-2 ν), the concomitant decrease of both bulk modulus and Poisson´s ratio are consistent with the elastic modulus data.

Hereafter, the deposition parameters utilized for the deposition of the Cr_2AlC samples presented in Figure 15 in **chapter 7** with the corresponding chemical compositions can be found. The samples shown in Figure 15 a and b were synthesized in an industrial-scale CemeCon CC800/9 deposition system at base pressures below 0.5 mPa utilizing a 50 x 8.8 cm² $Cr_{0.50}$-$Al_{0.27}$-$C_{0.23}$ composite target from Plansee Composite Materials GmbH. The MgO (100) substrates were mounted at a target-to-substrate distance of 50 (Figure 15 a) and 180 mm (Figure 15 b) and were heated to 560 – 590 °C. The gas flows during deposition were 100 (Figure 15 a) and 475 sccm (Figure 15 b) of Ar, resulting in deposition pressures of 0.19 and 1 Pa, respectively. A Melec HPPMS generator (SIPP2000USB-10-500-S) operating in a DC mode was used for powering the target with 2.3 (Figure 15 a) and 0.9 W/cm^2 (Figure 15 b). The deposition time was varied between 45 and 150 min, which resulted in film thicknesses of approximately 3.6 (Figure 15 a) and 0.5 µm (Figure 15 b). The sample shown in Figure 15 c and d were deposited in a lab-scale deposition system by DCMS at approxamatelly 600 °C substrate temperature. The base pressure was below 0.02 mPa and the Ar deposition pressure was 1.5 Pa. A 2“ $Cr_{0.5}$-$Al_{0.25}$-$C_{0.25}$ composite target (power density: 5 W/cm²) from Plansee Materials GmbH was facing the single-crystalline MgO (100) substrate at a distance of 12 cm and was sputtered for 66 (Figure 15 c) and 158 min (Figure 15 d) in order to obtain films with thicknesses of 500 and 1200 nm, respectively. Structural analysis of the deposited thin films was carried out by a Siemens D5000 system operating in a Bragg-Brentano mode and being equipped with a Cu radiation source operating at a voltage and current of 40 kV and 40 mA, respectively. The chemical composition was analyzed using a JEOL JSM-6480 scanning electron microscope with an EDAX Genesis 2000 energy dispersive X-ray spectroscopy device, utilizing an acceleration voltage 12 kV with a Cr_2AlC thin-film sample quantified by ERDA or EBS as a standard. The chemical compositions are depicted in Table S1.

Table S 1: Chemical composition of samples depicted in Figure 15.

Sample	**Cr [at.%]**	**Al [at.%]**	**C [at.%]**	**O [at.%]**
Figure 15 a	51.1	25.3	22.3	1.3
Figure 15 b	53.6	22.6	20.3	3.5
Figure 15 c	55.4	23.4	19.8	1.4
Figure 15 d	55.4	22.8	20.1	1.7

In the following, the deposition parameters utilized for the deposition of the VAlN sample presented in Figure 16 in **chapter 7** with the corresponding APT analysis parameters can be found. The VAlN sample was synthesized by HPPMS using a CemeCon CC800/9 system. The base pressure was below 0.6 mPa and two rectangular magnetrons with one elemental V (50 x 8.8 cm²) and one elemental Al target (50 x 8.8 cm²) were employed. One Si (100) substrate was mounted at a target-to-substrate distance of 180 mm and was heated to 480 °C. The angle between the substrate and each cathode was 23°. The gas flows during deposition were 160 sccm Ar and 80 sccm N_2 resulting in partial pressures of 294 and 149 mPa, respectively. Two Melec HPPMS generators (SIPP2000USB-10-500-S) with a frequency of 500 Hz, a duty cycle of 2.5% and a time-average power of 2400 W for the V target and 2200 W for the Al target were used, which resulted in peak power densities of approximately 465 W/cm² for the V target and 560 W/cm² for the Al target. A third Melec HPPMS generator was used for biasing the substrate. The substrate bias potential was varied during deposition from floating to -80 and -140 V and was applied in 200 µs long pulses. The compositional depth profile was obtained by 3D APT in a CAMECA LEAP 4000X HR. Laser-assisted pulsing with 30 pJ energy and 250 kHz is carried out for field evaporation at 60 K base temperature and >50 x 10^6 ions are collected at a detection rate of 0.5%. Specimen preparation is done by a standard lift-out procedure [137] and annular milling in a FEI HELIOS Nanolab 660 dual-beam focused ion beam microscope using Ga ions at 30 kV acceleration voltage to obtain a needle-like tip.

9. References

[1] P. Eklund, M. Beckers, U. Jansson, H. Högberg, L. Hultman, *Thin Solid Films* **518,** 1851 (2010).

[2] C. Walter, D.P. Sigumonrong, T. El-Raghy, J.M. Schneider, *Thin Solid Films* **515,** 389 (2006).

[3] J. Neidhardt, S. Mráz, J.M. Schneider, E. Strub, W. Bohne, B. Liedke, W. Möller, C. Mitterer, *Journal of Applied Physics* **104,** 063304 (2008).

[4] S. Mráz, J. Emmerlich, F. Weyand, J.M. Schneider, *Journal of Physics D: Applied Physics* **46,** 135501 (2013).

[5] L.R. Shaginyan, M. Mišina, S. Kadlec, L. Jastrabík, A. Macková, V. Peřina, *Journal of Vacuum Science & Technology A: Vacuum, Surfaces, and Films* **19,** 2554 (2001).

[6] S.M. Rossnagel, I. Yang, J.J. Cuomo, *Thin Solid Films* **199,** 59 (1991).

[7] C. Mitterer, *Journal of Solid State Chemistry* **133,** 279 (1997).

[8] P. Eklund, J. Emmerlich, H. Högberg, O. Wilhelmsson, P. Isberg, J. Birch, P.O.A. Persson, U. Jansson, L. Hultman, *Journal of Vacuum Science & Technology B: Microelectronics and Nanometer Structures* **23,** 2486 (2005).

[9] B.R. Rogers, T.C. J., T.S. Cale, *Journal of Vacuum Science & Technology B: Microelectronics and Nanometer Structures* **12,** 2980 (1994).

[10] D.B. Bergstrom, F. Tian, I. Petrov, J. Moser, J.E. Greene, *Applied Physics Letters* **67,** 3102 (1995).

[11] B.R. Rogers, T.S. Cale, Y.K. Chang, *Journal of Vacuum Science & Technology A: Vacuum, Surfaces, and Films* **14,** 1142 (1996).

[12] H. Ramarotafika, G. Lemperiere, *Thin Solid Films* **266,** 267 (1995).

[13] L.B. Jonsson, C. Hedlund, I.V. Katardjiev, S. Berg, *Thin Solid Films* **348,** 227 (1999).

[14] J. Frodelius, P. Eklund, M. Beckers, P.O.Å. Persson, H. Högberg, L. Hultman, *Thin Solid Films* **518,** 1621 (2010).

[15] P. Eklund, M. Beckers, J. Frodelius, H. Högberg, L. Hultman, *Journal of Vacuum Science & Technology A: Vacuum, Surfaces, and Films* **25,** 1381 (2007).

[16] P.O.Å. Persson, S. Kodambaka, I. Petrov, L. Hultman, *Acta Materialia* **55,** 4401 (2007).

[17] J. Willer, S. Pompl, D. Ristow, *Thin Solid Films* **188,** 157 (1990).

[18] R. Simão, *Thin Solid Films* **377-378,** 490 (2000).

[19] Y. Murakami, T. Shingyoji, *Journal of Vacuum Science & Technology A: Vacuum, Surfaces, and Films* **8,** 851 (1990).

[20] T. Yamazaki, N. Ikeda, H. Tawara, M. Sato, *Thin Solid Films* **235,** 71 (1993).

[21] M.Y. Liao, Y. Gotoh, H. Tsuji, J. Ishikawa, *Journal of Vacuum Science & Technology A: Vacuum, Surfaces, and Films* **23,** 1379 (2005).

[22] M.Y. Liao, Y. Gotoh, H. Tsuji, J. Ishikawa, *Journal of Vacuum Science & Technology B: Microelectronics and Nanometer Structures* **22,** L24 (2004).

[23] Y. Jiang, S. Mráz, J.M. Schneider, *Thin Solid Films* **538,** 1 (2013).

[24] A. Obrosov, R. Gulyaev, A. Zak, M. Ratzke, M. Naveed, W. Dudzinski, S. Weiss, *Materials* **10,** 156 (2017).

[25] C. Walter, C. Martinez, T. El-Raghy, J.M. Schneider, *steel research international* **76,** 225 (2005).

[26] J. Alami, P. Eklund, J. Emmerlich, O. Wilhelmsson, U. Jansson, H. Högberg, L. Hultman, U. Helmersson, *Thin Solid Films* **515,** 1731 (2006).

[27] M. Rausch, M. Pavlovič, P. Kreiml, M.J. Cordill, J. Winkler, C. Mitterer, *Applied Surface Science* **455,** 1029 (2018).

[28] J.-O. Achenbach, S. Mráz, D. Primetzhofer, J. Schneider, *Coatings* **9,** 206 (2019).

[29] M.W. Barsoum, *MAX Phases Properties of Machinable Ternary Carbides and Nitrides, Wiley-VCH Verlag GmbH, Weinheim, Germany* (2013).

[30] J.M. Schneider, D.P. Sigumonrong, D. Music, C. Walter, J. Emmerlich, R. Iskandar, J. Mayer, *Scripta Materialia* **57,** 1137 (2007).

[31] J.D. Hettinger, S.E. Lofland, P. Finkel, T. Meehan, J. Palma, K. Harrell, S. Gupta, A. Ganguly, T. El-Raghy, M.W. Barsoum, *Physical Review B* **72,** 115120 (2005).

[32] V. Podgursky, *Journal of Physics D: Applied Physics* **40,** 4021 (2007).

[33] M.W. Barsoum, T. El-Raghy, *Journal of the American Ceramic Society* **79,** 1953 (1996).

[34] T. El-Raghy, M.W. Barsoum, A. Zavaliangos, S.R. Kalidindi, *Journal of the American Ceramic Society* **82,** 2855 (2004).

[35] Z. Sun, Y. Zhou, M. Li, *Corrosion Science* **43,** 1095 (2001).

[36] H.J. Yang, Y.T. Pei, J.T.M. De Hosson, *Scripta Materialia* **69,** 203 (2013).

[37] L. Shen, D. Eichner, S. van der Zwaag, C. Leyens, W.G. Sloof, *Wear* **358-359,** 1 (2016).

[38] D. Eichner, A. Schlieter, C. Leyens, L. Shang, S. Shayestehaminzadeh, J.M. Schneider, *Wear* **402-403,** 187 (2018).

[39] Q. Huang, H. Han, R. Liu, G. Lei, L. Yan, J. Zhou, Q. Huang, *Acta Materialia* **110,** 1 (2016).

[40] S.H. Shah, P.D. Bristowe, *Scientific Reports* **7,** 9667 (2017).

[41] M.R. Field, P. Carlsson, P. Eklund, J.G. Partridge, D.G. McCulloch, D.R. McKenzie, M.M.M. Bilek, *Surface and Coatings Technology* **259,** 746 (2014).

[42] K. Macák, V. Kouznetsov, J. Schneider, U. Helmersson, I. Petrov, *Journal of Vacuum Science & Technology A: Vacuum, Surfaces, and Films* **18,** 1533 (2000).

[43] V. Kouznetsov, K. Macák, J.M. Schneider, U. Helmersson, I. Petrov, *Surface and Coatings Technology* **122,** 290 (1999).

[44] M. Hans, D. Music, Y.T. Chen, L. Patterer, A.O. Eriksson, D. Kurapov, J. Ramm, M. Arndt, H. Rudigier, J.M. Schneider, *Scientific Reports* **7,** 16096 (2017).

[45] D. Music, L. Banko, H. Ruess, M. Engels, A. Hecimovic, D. Grochla, D. Rogalla, T. Brögelmann, A. Ludwig, A. von Keudell, K. Bobzin, J.M. Schneider, *Journal of Applied Physics* **121,** 215108 (2017).

[46] W.D. Münz, *Journal of Vacuum Science & Technology A: Vacuum, Surfaces, and Films* **4,** 2717 (1986).

[47] P.H. Mayrhofer, D. Music, T. Reeswinkel, H.G. Fuß, J.M. Schneider, *Acta Materialia* **56,** 2469 (2008).

[48] P.H. Mayrhofer, D. Music, J.M. Schneider, *Journal of Applied Physics* **100,** 094906 (2006).

[49] A.E. Reiter, V.H. Derflinger, B. Hanselmann, T. Bachmann, B. Sartory, *Surface and Coatings Technology* **200,** 2114 (2005).

[50] D. McIntyre, J.E. Greene, G. Håkansson, J.E. Sundgren, W.D. Münz, *Journal of Applied Physics* **67,** 1542 (1990).

[51] S. Kolozsvári, P. Pesch, C. Ziebert, M. Stueber, S. Ulrich, *Plasma Processes and Polymers* **6,** S146 (2009).

[52] M. Liewald, S. Wagner, D. Becker, C. Ziebert, P. Pesch, S. Kolozsvári, *The International Journal of Advanced Manufacturing Technology* **58,** 495 (2011).

[53] G. Greczynski, S. Mráz, M. Hans, D. Primetzhofer, J. Lu, L. Hultman, J.M. Schneider, *Journal of Applied Physics* **121,** 171907 (2017).

[54] S.J. Rotert, D. Music, M. to Baben, J.M. Schneider, *Journal of Applied Physics* **113,** 083512 (2013).

[55] J.S.K.L. Gibson, S. Rezaei, H. Rueß, M. Hans, D. Music, S. Wulfinghoff, J.M. Schneider, S. Reese, S. Korte-Kerzel, *Materials Research Letters* **6,** 142 (2017).

[56] K.P. Shaha, H. Rueβ, S. Rotert, M. to Baben, D. Music, J.M. Schneider, *Applied Physics Letters* **103,** 221905 (2013).

[57] G. Greczynski, S. Mráz, H. Ruess, M. Hans, J. Lu, L. Hultman, J.M. Schneider, *Journal of Applied Physics* **122,** 025304 (2017).

[58] H. Ju, P. Jia, J. Xu, L. Yu, Y. Geng, Y. Chen, M. Liu, T. Wei, *Materials Chemistry and Physics* **215,** 368 (2018).

[59] A.B. Mei, R.B. Wilson, D. Li, D.G. Cahill, A. Rockett, J. Birch, L. Hultman, J.E. Greene, I. Petrov, *Journal of Applied Physics* **115,** 214908 (2014).

[60] I. Petrov, A. Myers, J.E. Greene, J.R. Abelson, *Journal of Vacuum Science & Technology A: Vacuum, Surfaces, and Films* **12,** 2846 (1994).

[61] J. Bohlmark, J. Alami, C. Christou, A.P. Ehiasarian, U. Helmersson, *Journal of Vacuum Science & Technology A: Vacuum, Surfaces, and Films* **23,** 18 (2005).

[62] H. Randhawa, P.C. Johnson, *Surface and Coatings Technology* **31,** 303 (1987).

[63] P.R. Willmott, J.R. Huber, *Reviews of Modern Physics* **72,** 315 (2000).

[64] D.M. Mattox, *Handbook of Physical Vapor Deposition (PVD) Processing, Elsevier Inc., Oxford* (2010).

[65] A. Anders, *Surface and Coatings Technology* **205,** S1 (2011).

[66] M.N. Drozdov, S.V. Gaponov, S.A. Gusev, E.B. Kluenkov, V.I. Luchin, D.V. Masterov, S.K. Saykov, A.K. Vorobiev, *IEEE Transactions on Appiled Superconductivity* **9,** 2371 (1999).

[67] Y.H. Jo, B.C. Mohanty, D.H. Yeon, S.M. Lee, Y.S. Cho, *Solar Energy Materials and Solar Cells* **132,** 136 (2015).

[68] R.R. Olson, M.E. King, G.K. Wehner, *Journal of Applied Physics* **50,** 3677 (1979).

[69] P.H. Dawson, *Quadrupole Mass Spectrometry and its applications, Elsevier Scientific Publishing Company, Amsterdam* (1976).

[70] J.I. Goldstein, C.E. Lyman, D.E. Newbury, E. Lifshin, P. Echlin, L. Sawyer, D.C. Joy, J.R. Michael, *Scanning Electron Microscopy and X-Ray Microanalysis, Kluwer Academic / Plenum, New York* (2003).

[71] G. Friedbacher, H. Bubert, *Surface and Thin Film Analysis, WILEY-VCH, Weinheim* (2011).

[72] M. Birkholz, *Thin Film Analysis by X-Ray Scattering, WILEY-VCH, Weinheim* (2006).

[73] W.C. Oliver, G.M. Pharr, *Journal of Materials Research* **7,** 1564 (1992).

[74] A.C. Fischer-Cripps, *The IBIS Handbook of Nanoindentation, Fischer-Cripps Laboratories, Forestville* (2013).

[75] W. Kohn, *Reviews of Modern Physics* **71,** 1253 (1999).

[76] F. Birch, *Journal of Geophysical Research* **83,** 1257 (1978).

[77] D. Music, T. Takahashi, L. Vitos, C. Asker, I.A. Abrikosov, J.M. Schneider, *Applied Physics Letters* **91,** 191904 (2007).

[78] W. Voigt, *Lehrbuch der Kristallphysik, Teubner, Berlin* (1928).

[79] A. Reuss, *ZAMM - Zeitschrift für Angewandte Mathematik und Mechanik* **9,** 49 (1929).

[80] R. Hill, *Proceedings of the Physical Society. Section A* **65,** 349 (1952).

[81] P. Söderlind, L. Nordström, Y. Lou, B. Johansson, *Physical Review B* **42,** 4544 (1990).

[82] J.M. Schneider, B. Hjörvarsson, X. Wang, L. Hultman, *Applied Physics Letters* **75,** 3476 (1999).

[83] H.F. Winters, E. Kay, *Journal of Applied Physics* **38,** 3928 (1967).

[84] M. Ohring, *The materials science of thin films, Academic Press, San Diego* (2001).

[85] S. Berg, I.V. Katardjiev, *Journal of Vacuum Science & Technology A: Vacuum, Surfaces, and Films* **17,** 1916 (1999).

[86] A. Anders, *Applied Physics Letters* **80,** 1100 (2002).

[87] G. Greczynski, I. Petrov, J.E. Greene, L. Hultman, *Vacuum* **116,** 36 (2015).

[88] L. Shang, P. Konda Gokuldoss, S. Sandlöbes, M. to Baben, J.M. Schneider, *Journal of the European Ceramic Society* **37,** 1339 (2017).

[89] B. Stelzer, X. Chen, P. Bliem, M. Hans, B. Völker, R. Sahu, C. Scheu, D. Primetzhofer, J.M. Schneider, *Scientific Reports* **9,** 8266 (2019).

[90] E.R. Rauch, A. Duft, *Icotom 14: Textures of Materials, Pts 1and 2* **495-497,** 197 (2005).

[91] E.R. Rauch, M. Véron, J. Portillo, D. Bultreys, Y. Maniette, S. Nicolopoulos, *Microscopy and Analysis* **93,** S5 (2008).

[92] E.F. Rauch, J. Portillo, S. Nicolopoulos, D. Bultreys, S. Rouvimov, P. Moeck, *Zeitschrift für Kristallographie* **225,** (2010).

[93] K. Momma, F. Izumi, *Journal of Applied Crystallography* **44,** 1272 (2011).

[94] Z. Sun, S. Li, R. Ahuja, J.M. Schneider, *Solid State Communications* **129,** 589 (2004).

[95] P. Hohenberg, W. Kohn, *Physical Review* **136,** B864 (1964).

[96] G. Kresse, *Journal of Non-Crystalline Solids* **192-193,** 222 (1995).

[97] G. Kresse, J. Hafner, *Physical Review B* **49,** 14251 (1994).

[98] G. Kresse, D. Joubert, *Physical Review B* **59,** 1758 (1999).

[99] J.P. Perdew, K. Burke, M. Ernzerhof, *Physical Review Letters* **77,** 3865 (1996).

[100] P.E. Blöchl, O. Jepsen, O.K. Andersen, *Physical Review B* **49,** 16223 (1994).

[101] H.J. Monkhorst, J.D. Pack, *Physical Review B* **13,** 5188 (1976).

[102] A. Abdulkadhim, M.t. Baben, T. Takahashi, V. Schnabel, M. Hans, C. Polzer, P. Polcik, J.M. Schneider, *Surface and Coatings Technology* **206,** 599 (2011).

[103] F. Herrig, D. Music, H. Rueß, A.L. Ravensburg, P.J. Pöllmann, J.M. Schneider, *Scripta Materialia* **153,** 49 (2018).

[104] R. Mertens, Z. Sun, D. Music, J.M. Schneider, *Advanced Engineering Materials* **6,** 903 (2004).

[105] *Joint Committee on Powder Diffraction Standards (JCPDS), International Centre for Diffraction Data, Newtown Square, PA, USA*.

[106] I. Petrov, P.B. Barna, L. Hultman, J.E. Greene, *Journal of Vacuum Science & Technology A: Vacuum, Surfaces, and Films* **21,** S117 (2003).

[107] H. Rueß, M. to Baben, S. Mráz, L. Shang, P. Polcik, S. Kolozsvári, M. Hans, D. Primetzhofer, J.M. Schneider, *Vacuum* **145,** 285 (2017).

[108] H.S. Kim, M.B. Bush, *Nanostructured Materials* **11,** 361 (1999).

[109] Y.L. Du, Z.M. Sun, H. Hashimoto, M.W. Barsoum, *Journal of Applied Physics* **109,** (2011).

[110] M. Ramzan, S. Lebègue, R. Ahuja, *physica status solidi (RRL) - Rapid Research Letters* **5,** 122 (2011).

[111] P. Zhu, F. Ge, S. Li, Q. Xue, F. Huang, *Surface and Coatings Technology* **232,** 311 (2013).

[112] B.D. Fulcher, X.Y. Cui, B. Delley, C. Stampfl, *Physical Review B* **85,** 184106 (2012).

[113] J.P. Perdew, Y. Wang, *Physical Review B* **45,** 13244 (1992).

[114] R. Dronskowski, P.E. Bloechl, *The Journal of Physical Chemistry* **97,** 8617 (1993).

[115] V.L. Deringer, A.L. Tchougreeff, R. Dronskowski, *Journal of Physical Chemistry A* **115,** 5461 (2011).

[116] S. Maintz, V.L. Deringer, A.L. Tchougreeff, R. Dronskowski, *Journal of Computational Chemistry* **37,** 1030 (2016).

[117] V.I. Ivashchenko, P.E.A. Turchi, V.I. Shevchenko, E.I. Olifan, *Physical Review B* **84,** 174108 (2011).

[118] B.A. Ravan, M. Faghihnasiri, H. Jafari, *Materials Chemistry and Physics* **228,** 237 (2019).

[119] M. to Baben, L. Raumann, D. Music, J.M. Schneider, *Journal of Physics: Condensed Matter* **24,** 155401 (2012).

[120] H. Euchner, P.H. Mayrhofer, *Surface and Coatings Technology* **275,** 214 (2015).

[121] E.I. Isaev, S.I. Simak, I.A. Abrikosov, R. Ahuja, Y.K. Vekilov, M.I. Katsnelson, A.I. Lichtenstein, B. Johansson, *Journal of Applied Physics* **101,** 123519 (2007).

[122] W. Weber, P. Roedhammer, L. Pintschovius, W. Reichardt, F. Gompf, A.N. Christensen, *Physical Review Letters* **43,** 868 (1979).

[123] F. Kubel, W. Lengauer, K. Yvon, K. Knorr, A. Junod, *Physical Review B* **38,** 12908 (1988).

[124] N. Koutná, D. Holec, O. Svoboda, F.F. Klimashin, P.H. Mayrhofer, *Journal of Physics D: Applied Physics* **49,** 375303 (2016).

[125] G. Greczynski, S. Mráz, L. Hultman, J.M. Schneider, *Applied Physics Letters* **108,** 041603 (2016).

[126] F.P. Knudsen, *Journal of the American Ceramic Society* **45,** 94 (1962).

[127] F. Tasnádi, I.A. Abrikosov, L. Rogström, J. Almer, M.P. Johansson, M. Odén, *Applied Physics Letters* **97,** 231902 (2010).

[128] J.M. Schneider, A. Anders, B. Hjörvarsson, I. Petrov, K. Macák, U. Helmersson, J.-E. Sundgren, *Applied Physics Letters* **74,** 200 (1999).

[129] M.V. Moro, R. Holeňák, L.Z. Medina, U. Jansson, D. Primetzhofer, *Thin Solid Films* 137416 (2019).

[130] M. Hans, M. to Baben, Y.-T. Chen, K.G. Pradeep, D.M. Holzapfel, D. Primetzhofer, D. Kurapov, J. Ramm, M. Arndt, H. Rudigier, J.M. Schneider, *Surface and Coatings Technology* **305,** 249 (2016).

[131] M. Naveed, A. Obrosov, A. Zak, W. Dudzinski, A. Volinsky, S. Weiß, *Metals* **6,** (2016).

[132] R. Su, H. Zhang, X. Meng, L. Shi, C. Liu, *Fusion Engineering and Design* **125,** 562 (2017).

[133] R. Daniel, J. Keckes, I. Matko, M. Burghammer, C. Mitterer, *Acta Materialia* **61,** 6255 (2013).

[134] D.V. Shtansky, P.V. Kiryukhantsev-Korneev, A.N. Sheveyko, B.N. Mavrin, C. Rojas, A. Fernandez, E.A. Levashov, *Surface and Coatings Technology* **203,** 3595 (2009).

[135] H. Bolvardi, J. Emmerlich, S. Mráz, M. Arndt, H. Rudigier, J.M. Schneider, *Thin Solid Films* **542,** 5 (2013).

[136] D. Music, L. Banko, H. Ruess, M. Engels, A. Hecimovic, D. Grochla, D. Rogalla, T. Brögelmann, A. Ludwig, A. von Keudell, K. Bobzin, J.M. Schneider, *Journal of Applied Physics* **121,** (2017).

[137] T.F. Kelly, D.J. Larson, *Annual Review of Materials Research* **42,** 1 (2012).